

We are IntechOpen, the world's leading publisher of Open Access books Built by scientists, for scientists

6,900

Open access books available

185,000

International authors and editors

200M

Downloads

Our authors are among the

154

Countries delivered to

TOP 1%

most cited scientists

12.2%

Contributors from top 500 universities



WEB OF SCIENCE™

Selection of our books indexed in the Book Citation Index
in Web of Science™ Core Collection (BKCI)

Interested in publishing with us?
Contact book.department@intechopen.com

Numbers displayed above are based on latest data collected.
For more information visit www.intechopen.com



Silicon Photo Multipliers Detectors Operating in Geiger Regime: an Unlimited Device for Future Applications

Giancarlo Barbarino, Riccardo de Asmundis, Gianfranca De Rosa,
Carlos Maximiliano Mollo, Stefano Russo and Daniele Vivolo
*Università di Napoli "Federico II" - Departement of Physics Sciences
and Istituto Nazionale di fisica nucleare - Section of Napoli
Italy*

1. Introduction

Photon detectors are indispensable in many areas of fundamental physics research, particularly in the emerging fields of particle astrophysics, nuclear and particle physics, as well as in medical equipment (i.e. PET), in physical check-ups and diagnosis as in-vitro inspection (Radioimmunoassay and Enzyme immunoassay as luminescent, fluorescent, Chemiluminescent Immunoassay), biomedicine, industrial application, in environmental measurement equipment (like dust counters used to detect dust contained in air or liquids, and radiation survey monitors used in nuclear power plants). In astroparticle physics, photons detectors play a crucial role in the detection of fundamental physical processes: in particular, most of the future experiments which aimed at the study of very high-energy (GRB, AGN, SNR) or extremely rare phenomena (dark matter, proton decay, zero neutrinos-double beta decay, neutrinos from astrophysical sources)[3-7] are based on photons detection. The needs of very high sensitivity push the designing of detectors whose sizes should greatly exceed the dimensions of the largest current installations. In the construction of such large-scale detectors no other option remains as using natural media - atmosphere, deep packs of ice, water and liquefied gases at cryogenic temperatures [8-13]. In these (transparent) media, charged particles, originating from interaction or decays of primary particles, emit Cherenkov radiation or fluorescence light, detected by photosensitive devices. Hence, for the improvement in the quality of the experimental results a particular attention should be paid to the improvement of photon detectors performances. In underwater neutrino telescopes (but this is applicable also to other experiments) Cherenkov light, emitted by charged leptons stemming from neutrino interaction, hits photomultipliers (PMT) situated at different distances from the track. This implies, that the response of PMTs should be linear in a very wide range from high illumination to the single photon. Another area of interest is the direct searches of Dark Matter in form of WIMPs: in these experiments it is exploited the scintillation properties of double-phase (liquid-gas) detectors, where primary and secondary scintillation light signals are detected by high-efficiency PMTs, immersed in cryogenic liquids or low temperature gases (89 K for the liquid argon) [14-17]. The next generation of experiments requires further improvement in linearity, gain, and sensitivity (quantum efficiency and single photon counting capability) of PMTs.

To date, the photon detection capabilities of the Vacuum Photomultiplier Tube (VPMT) seem to be unrivalled. Nevertheless standard photomultiplier tubes suffer of the following drawbacks:

- fluctuations in the first dynode gain make single photon counting difficult;
- the linearity is strongly related to the gain and decreases as the latter increases;
- the transit time spreads over large fluctuations;
- the mechanical structure is complex and expensive;
- they are sensitive to the magnetic fields;
- the need of voltage dividers increases failure risks, complexity in the experiments designs and power consumption.

2. Alternatives to the standard photomultipliers tubes

To overcome these limitations, alternatives to VPMT, mainly concentrated on solid-state detectors, are under study. After about one century of standard technology (photocathode and dynode electron multiplication chain), the recent strong developments of modern silicon devices have the potential to boost this technology towards a new generation of photodetectors, based on an innovative and simple inverse p-n junction, PN or PIN photodiodes, avalanche photodiodes—APD and avalanche photodiodes in linear Geiger-mode (GM-APD, SiPM from now on) [18-25]. These solid-state devices present important advantages over the vacuum ones, namely higher quantum efficiency, lower operation voltages, insensitivity to the magnetic fields, robustness and compactness. The step by-step evolution of solid-state photon detectors was mainly determined by their internal gain: a PIN has no gain, an APD can reach a gain of few hundreds, while the GM-APD 10^5 – 10^6 , comparable with that of the vacuum photodetectors; this would allow the GM-APD to achieve single-photon sensitivity and to be used in low-level light applications. This silicon device has become commercially available in the recent years.

We will first discuss the detection of light by silicon devices and then move on to the description of the SiPM and its properties and possible applications.

2.1 Light detection with the photodiode

The basis for detection of light in silicon photodiodes is the p-n junction described in Figure 1, where a depleted region is formed due to carriers diffusion [26].

A junction is formed by diffusing a donor impurity to a shallow depth into silicon which is originally high purity p-type, sometimes called π -type silicon. Thus the layer at the surface is highly doped n-type, often referred as n^+ type with an high concentration of electrons, and the material inside is p type with a relatively low concentration of holes. A schematic view of the structure is shown in Figure 2. The resulting structure, referred to as an n^+ -p junction, presents a configuration $n^+p\pi p^+$, where π is a very slight p-type doping. In an analogous fashion a diffused p^+n junction detector can be constructed. Since the density of acceptors in the p-type region is much lower relatively to that of donors in the n^+ -type region, the space charge region extends much further into the p region than into the n^+ region. This space-charge region, characterized primarily by acceptor centres in the p-region and filled by donor electrons from the n^+ region, is a charge depleted region of very high resistivity. If electron-hole pairs are produced in this region, the electric field will drive electrons toward the n and holes toward the p side producing a current through the device.

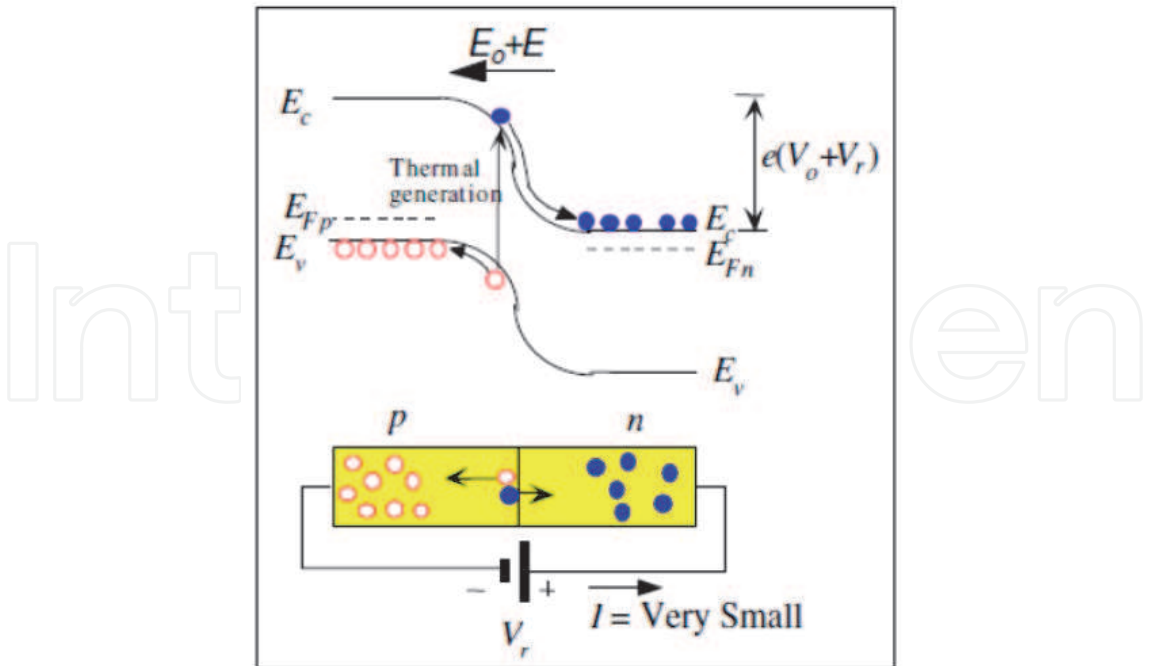


Fig. 1. p-n junction with reversed bias. Energy band diagram is also shown.

2.2 Photon absorption in silicon

Pairs can be produced by light if the energy of the photon is sufficient to bring the electron over the energy band gap.

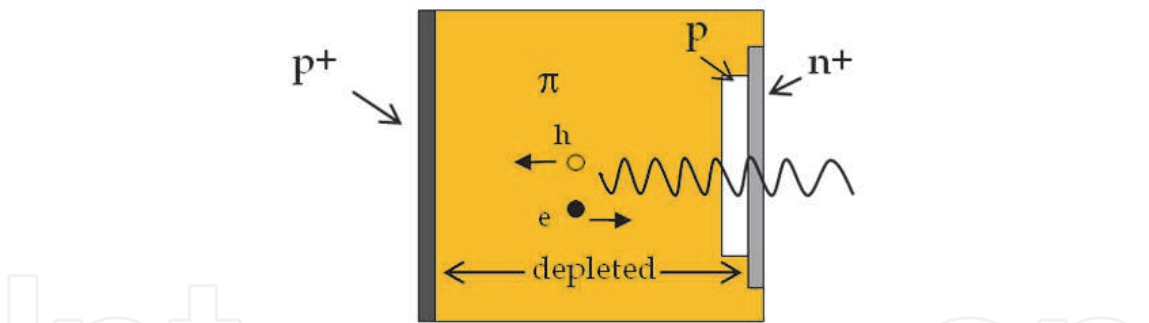


Fig. 2. Schematic view of a p+n junction.

The photon absorption process for photo generation, that is the creation of electron-hole pairs, requires the photon Energy to be at least equal to the band gap energy E_{gap} of the semiconductor material to excite an electron from the valence to the conduction band, namely $h\nu > E_{gap}$, corresponding to $hc/\lambda > E_{gap}$:

$$E_{ph} = h\nu = \frac{hc}{\lambda} > E_{gap}$$

The upper cut-off wavelength (or the threshold wavelength) λ_{th} is therefore determined by the bandgap energy E_{gap} :

$$\lambda_{th}(\mu m) = \frac{hc}{E_{gap}} = \frac{1.24}{E_{gap}(eV)} \tag{1}$$

In some semiconductors, such as Si and Ge, the photon absorption process for photon energies near E_{gap} requires the absorption and emission of lattice vibrations (vibrations of the Si atoms), namely phonons. The absorption process is said, in these cases, to be indirect as it depends on lattice vibrations which in turn depends on the temperature [27]. Since the interaction of a photon with a valence electron needs a third body, a lattice vibration, the probability of photon absorption is not as high as in a direct transition. As a consequence, the threshold wavelength is not as sharp as for direct band gap semiconductors. During the absorption process, a phonon may be absorbed or emitted. If ξ is the frequency of the lattice vibrations, then the phonon energy is $h\xi$ and the photon energy should be $h\nu > E_{\text{gap}} \pm h\xi$. Actually, since $h\xi$ is small (<0.1 eV), the energy needed for absorption is very close to E_{gap} . In silicon, for which $E_{\text{gap}}=1.12$ eV, the threshold wavelength as given by the Equation 1 is ≈ 1100 nm.

Incident photons with wavelengths shorter than λ_{th} become absorbed as they travel in the semiconductor and the light intensity, which is proportional to the number of photons, decays exponentially with distance into the semiconductor. The absorption coefficient α determines how far into a material the light of a particular wavelength can penetrate before absorption. In a material with a low absorption coefficient, light is only poorly absorbed, and if the material is thin enough, it will appear transparent to that wavelength.

The absorption coefficient, α , is related to the extinction coefficient, k , by the following formula:

$$\alpha = \frac{4\pi k}{\lambda}$$

where λ is the wavelength. Thus, defining the complex index of refraction as $\tilde{n} = n - ik$, the imaginary component k is related to the absorption, whereas the real component $n = c/v_{\text{phase}}$ is related to reflectivity. In Figure 3 the real and imaginary part of the refractive index of silicon is shown [28].

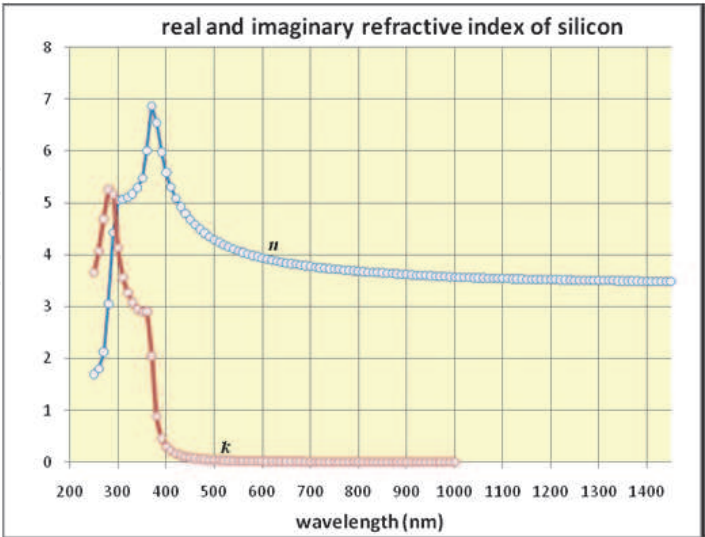


Fig. 3. Real and (negative) imaginary components of the refractive index for silicon at 300 K.

As a consequence of the cut-off wavelength, direct bandgap semiconductor materials (as GaAs, InP) have a sharp edge in their absorption coefficient. Actually, even for those

photons which have an energy above the band gap, the absorption coefficient is not constant, but still depends strongly on the wavelength. The probability of absorbing a photon depends on the probability that a photon and an electron interact in such a way as to move from one energy band to another. For photons which have an energy very close to that of the band gap, the absorption is relatively low since only those electrons directly at the valence band edge can interact with the photon to cause absorption. As the photon energy increases a larger number of electrons can interact with the photon, resulting in a higher absorption probability.

In indirect bandgap semiconductor materials, like silicon, there is a long tail in absorption out to long wavelengths. Figure 4 [27] shows the absorption coefficient α as a function of wavelength λ for various semiconductors: it is clear the different behaviour of α with the wavelength in the case of direct band gap semiconductors (e.g. GaAs, InP) with respect to indirect band gap semiconductors (e.g. Si, Ge). In Figure 5 [29], instead, the absorption length or penetration depth, defined as $1/\alpha$, as a function of wavelength for Si is shown.

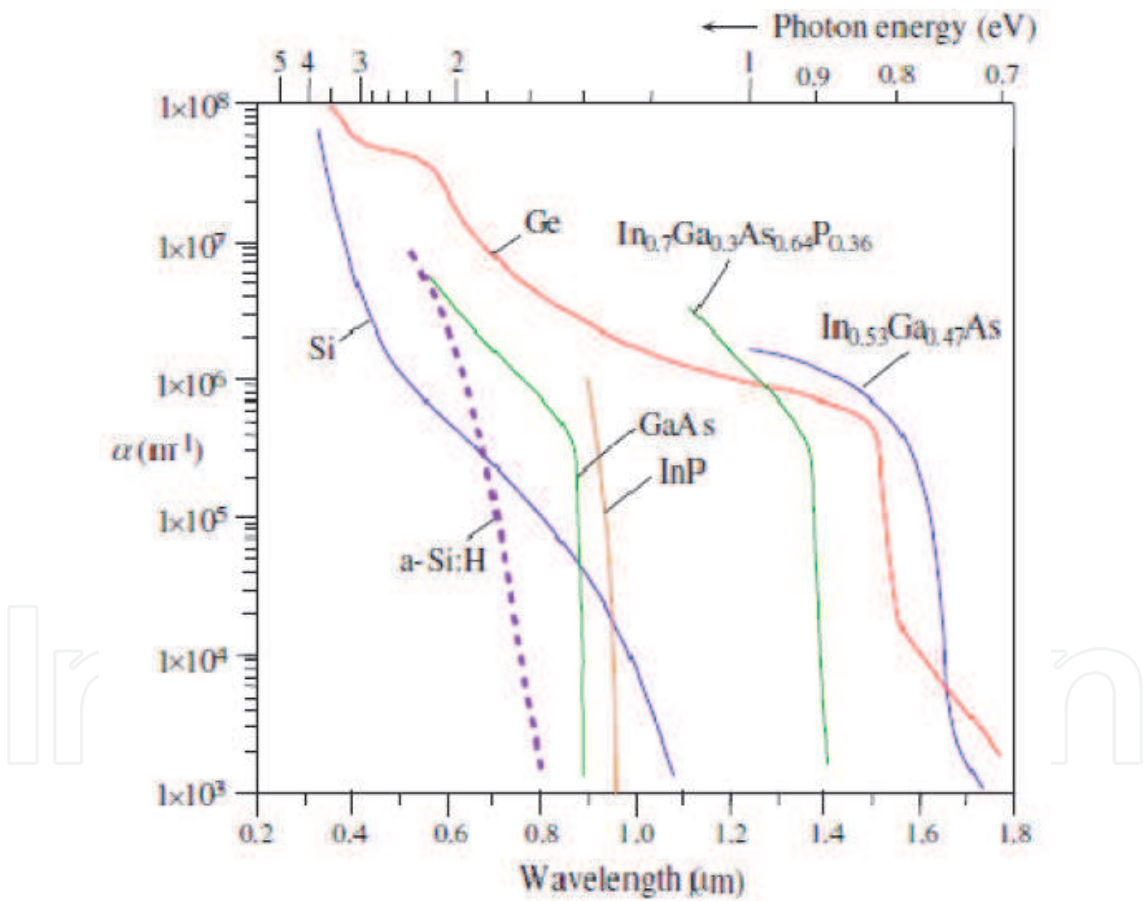


Fig. 4. Absorption coefficient α as a function of wavelength λ for various semiconductors.

To detect light by a photodiode, it first has to enter through the surface and then absorbed in the active volume of the device. Due to the high value of real part of the refractive index of silicon, which is above 3.5 for wavelengths below 1100 nm at 300 K as shown in Figure 3, an antireflective coating is needed to reduce the strong Fresnel reflection of light from the surface of the device.

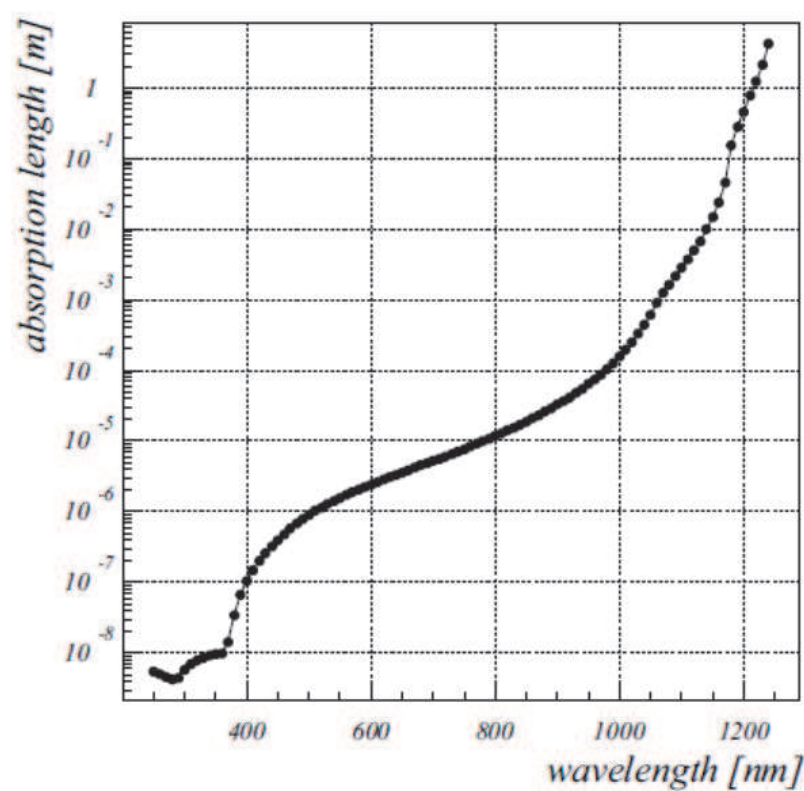


Fig. 5. Absorption length $1/\alpha$ as a function of wavelength λ for Silicon.

Actually, not all the incident photons are absorbed to create pairs that can be collected and give rise to a photocurrent. The efficiency of the conversion process is measured by the quantum efficiency QE of the detector, defined as

$$QE = \frac{\text{number of electron – hole pairs generated and collected}}{\text{number of incident photons}}$$

which depends on the wavelength. In the evaluation of QE, the number of electrons collected per seconds is given by I_{ph}/e , where I_{ph} is the measured photocurrent, whereas the number of photons arriving per second is $P_o/h\nu$, with P_o the incident optical power. Then the QE can be also defined as [27]

$$QE = \frac{I_{ph} / e}{P_o / h\nu}$$

A typical photodiode QE is shown in Figure 6 [30]. If the semiconductor length is comparable with the penetration depth not all the photons will be absorbed, resulting in a low QE. Therefore, to obtain an high quantum efficiency, the thickness of the depleted layer has to be larger than the absorption length. The absorption length shows strong variations from about 10 nm, for near UV light, to more than 1 mm, in the infrared region. To enhance the sensitivity in the range of blue light, the active region needs to be close to the surface and for the detection of longer wavelengths it has to be thick compared to the absorption length.

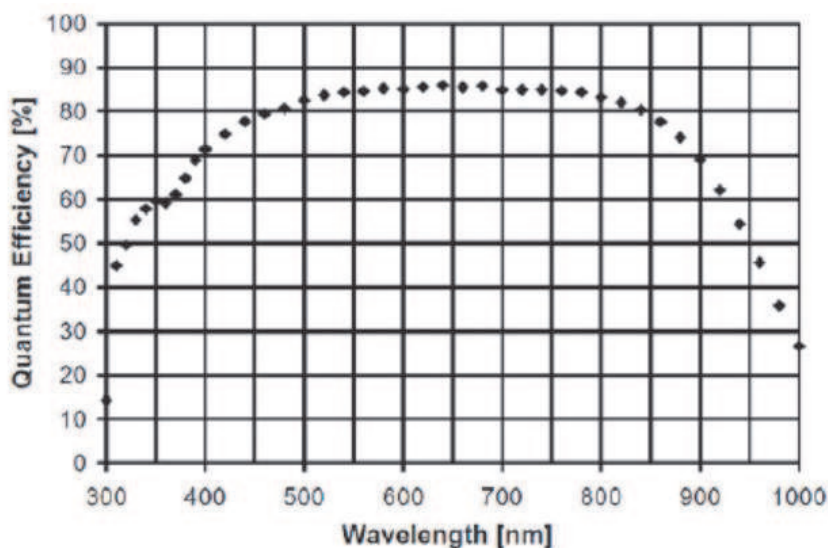


Fig. 6. Typical photodiode QE as a function of wavelength.

2.3 Reverse biased photodiodes

The thickness of the layer can be increased by applying a reverse bias to the diode junction. To obtain a thick depletion layer with low reverse bias, a PIN photodiode is used with an intrinsic layer between the p and n faces of the diode. The photodiode does not present any internal amplification of the signal so the number of charges generated is equal to the number of detected photons. It can be used for applications in which more than about 10,000 photons are simultaneously detected by the device. Taking into account that the capacitance per unit area C/A , expressed in picofarad per square centimetre, is $C/A = 1,061/x_0$ where x_0 is the depletion layer thickness expressed in cm, millivolt ranged signal is expected using typical parameters [31]. A typical application in high energy physics for such a device is the calorimetry, in which a large amount of photons has to be detected.

To detect weaker signals, instead, internal amplification is required. This can be obtained, as in gas based devices, by increasing the applied voltage. In fact, if the electric field in the silicon is high enough, primary carriers can produce new pairs by impact ionization. These generated electron-hole pairs are further accelerated by the electric field to a sufficiently high kinetic energy to cause new impact ionization, releasing more electron-hole pairs, which leads to an avalanche of impact ionization processes. Thus, with a single photon absorption, one can generate a large number of electron-hole pairs, all of which contribute to the observed photocurrent, leading an internal gain mechanism. Each absorbed photon creates in average a finite number M of electron-hole pairs exploiting the impact ionization process. The multiplication of carriers in the avalanche region depends on the probability of impact ionization which strongly depends on the reverse bias V_{bias} .

This mode of operation is called linear because the number of the collected carriers is proportional (by a factor M) to the number of absorbed photons. A photodiode with such an amplification region is called the avalanche photodiode (APD). The ionization rate is higher for electrons than for holes, so the amplification process for electrons starts at lower fields and the avalanche grows in the direction of the electrons movement. With the increase in the electric field also holes start to ionize. When the ionization probability is high enough, the amplification can no longer be controlled. This limits the amplification factor in APDs to about ~ 100 . Due to the low amplification, these devices are still not appropriate for detection

of signals of a few photons only. However, signals coming from about 100 photons can be detected.

2.4 Geiger mode APD silicon photomultiplier

To obtain the single photon sensitivity in a silicon device, one needs to operate the APD in the Geiger mode [32]. A diode working in a region near the breakdown voltage can be operated in two different ways depending on whether the bias voltage is below or above the breakdown point. In the first case the device is called avalanche photodiode (APD) described above. In the second case the device is referred to as Geiger-mode APD (GM-APD). In this bias condition, the electric field is so high that a single carrier injected into the depletion region can trigger a self-sustaining avalanche. The carrier initiating the discharge can be either thermally generated (noise source of the device) or photo-generated (useful signal).

In Figure 7 the schematic view of the gain as a function of reverse bias is shown.

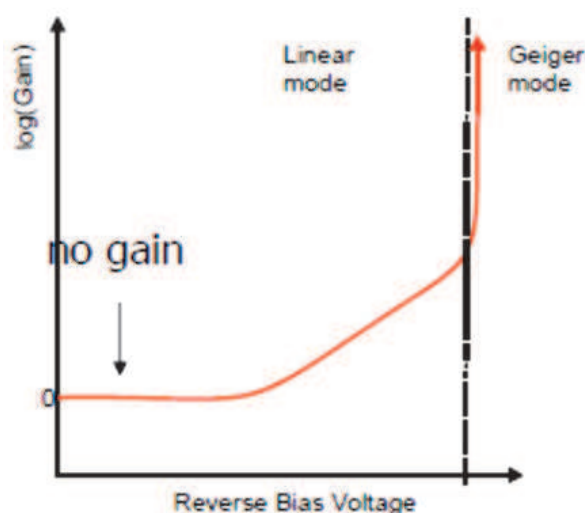


Fig. 7. Schematic view of gain as a function of V_{bias} .

The main limitation of a single diode working in GM is that the output signal is the same regardless of the number of interacting photons. In order to overcome this limitation, the diode can be segmented in tiny micro-cells (each working in GM) connected in parallel to a single output. Each element, when activated by a photon, gives the same current response, so that the output signal is proportional to the number of cells hit by a photon and the output signal is the sum of the Geiger mode signals of microcells. The dynamic range is limited by the number of elements composing the device, and the probability that two or more photons hit the same micro-cell depends on the size of the micro-cell itself. This structure is called Silicon Photo Multiplier (SiPM) [1].

All the microcells are identical, independent and operate in single photon counting mode. A quenching mechanism is implemented thanks to a specially resistive material technology. Together with the common electrode structure all this gives the possibility to act as a proportional detector for measurements of low intensity photons flux.

The typical density of microcells that can be produced is 1000–5000 per mm^2 and the total number of microcells on our tested photodetectors with sensitive area of 1 mm^2 is of the order of 2000. This defines the dynamic range of the device. The noise conditions of the

SiPM is defined by dark count rate, as in Geiger mode a single thermally generated electron or hole can initiate an avalanche, leading to an electrical pulse that is indistinguishable from the one of a single photon. This gives the main limitation of increasing the sensitive area of SiPM operated in single photon counting mode, but it is not so significant for low photon flux measurement when $N_{\text{phot}} > 3$.

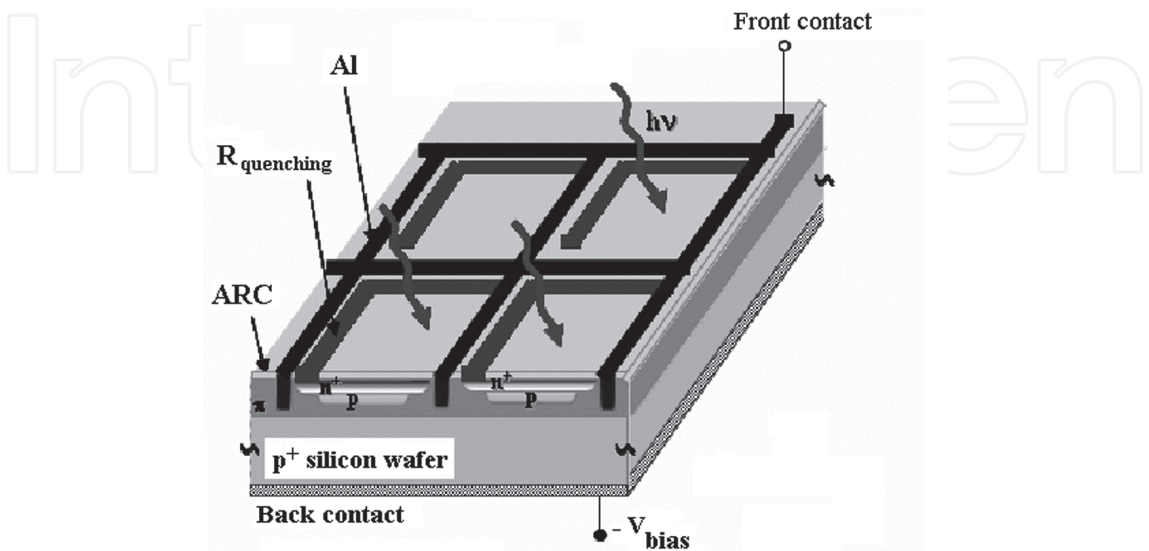


Fig. 8. Structure of the multi cell matrix of a SiPM.

3. Structure of the SiPM

The structure of the silicon photomultiplier is a combination of large number of avalanche microcells on a single substrate and with common quenching mechanism (resistive layer) and common electrodes.

3.1 Structure of avalanche microcell

The schematic structure of the avalanche microcell of a SiPM is shown in Figure 9 and presents a configuration $n^+-p-\pi-p^+$, where π represents very slight p-type doping.

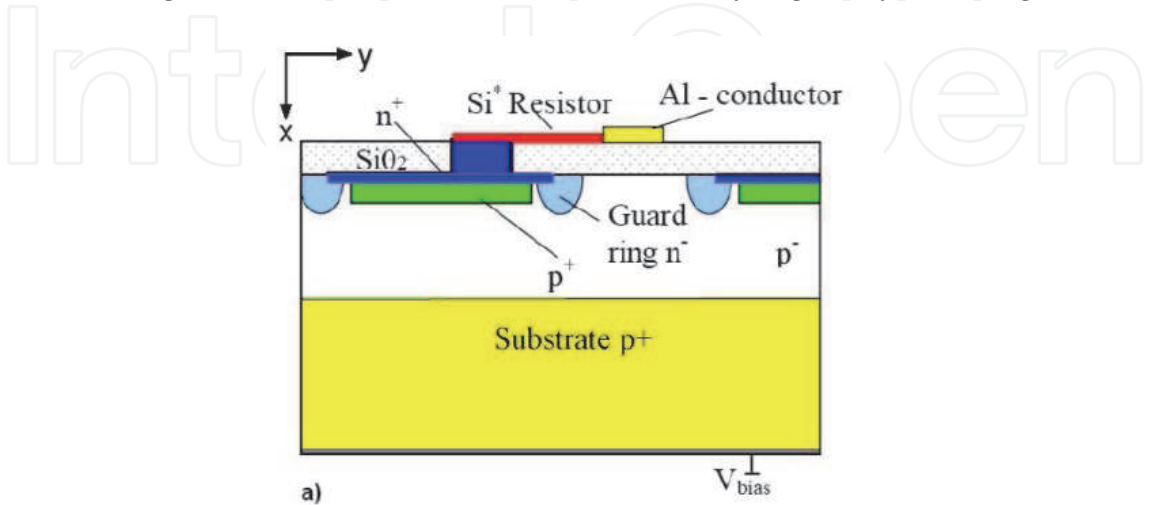


Fig. 9. Schematic structure of avalanche microcell of SiPM.

The n^+ side is thin and is the one which receives light through a window. A thickness of about $1\mu\text{m}$ of depletion region between the thin n^+ (thickness = $0.1\text{--}1.5\mu\text{m}$) and p layers is created thanks to the reverse electric field. There are three p-type layers of different doping levels next to the n^+ layer to suitably modify the field distribution across the structure. The first is a thin p-type layer, the second is a thick lightly p-type doped (almost intrinsic) π -layer of $\approx 300\mu\text{m}$, and the third is a heavily doped p^+ layer $\approx 3\mu\text{m}$ thick. On the surface of the avalanche microstructure a thin metal layer is placed ($\approx 0.01\mu\text{m}$) with an antireflection coating. Above the n^+ region, a resistive SiO_2 layer (thickness $\approx 0.15\mu\text{m}$, $\rho \approx 10^5\text{--}10^7\Omega\text{cm}$) limits the Geiger breakdown propagation by a local reduction of the electric field. The electric field is at a maximum at the n^+p junction, then decreases slowly through the p-layer. The field vanishes at the end of the narrow depletion layer in the p^+ side, as shown in Figure 10 [33].

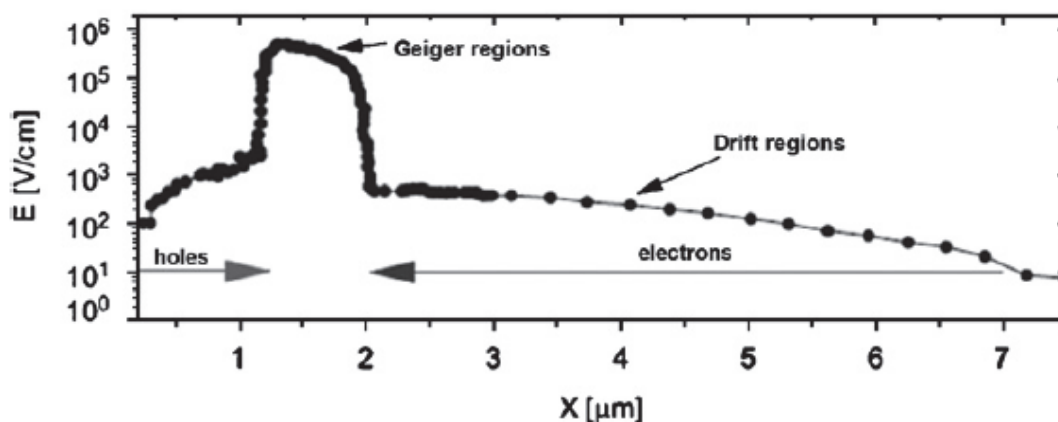


Fig. 10. Configuration of the electric field. The high-field region ($E \approx 5 \times 10^5 \text{ V/cm}$) is built up in the highly doped n^+p .

The absorption of photons of $\lambda \approx 400 \text{ nm}$ takes place mainly in the π -layer. The nearly uniform field here separates the electron-hole pairs and drifts them at velocities near saturation towards the n^+ and p^+ sides, respectively. When the drifting electrons reach the p-layer it may be accelerated by the high fields to sufficiently large kinetic energies to further cause impact ionization and release more electron-hole pairs which leads to an avalanche of impact ionization processes. Thus, from a single electron entering the p-layer, one can generate a large number of electron-hole pairs all of which contribute to the observed photocurrent. In this mode, any electron event in the sensitive area will produce a very large current flow with amplification gain of up to 10^6 .

3.2 Operation principle of a SiPM

As mentioned in the previous paragraph the SiPM is a matrix of GM-APDs connected in parallel. A schematic representation of the device is shown in Figure 11. The connection between the cells is made on one side by the low-resistivity substrate and on the other side by a metal layer. The diodes (labelled as D) are asymmetric p-n junctions. Each GM-APD has in series a quenching resistor (R_Q) which is needed to stop the avalanche current and, then, to restore the initial bias condition enabling the detection of a new incoming photon. A reverse bias voltage (V_{bias}) is applied to each junction through the common substrate electrode to deplete the n^+p junctions.

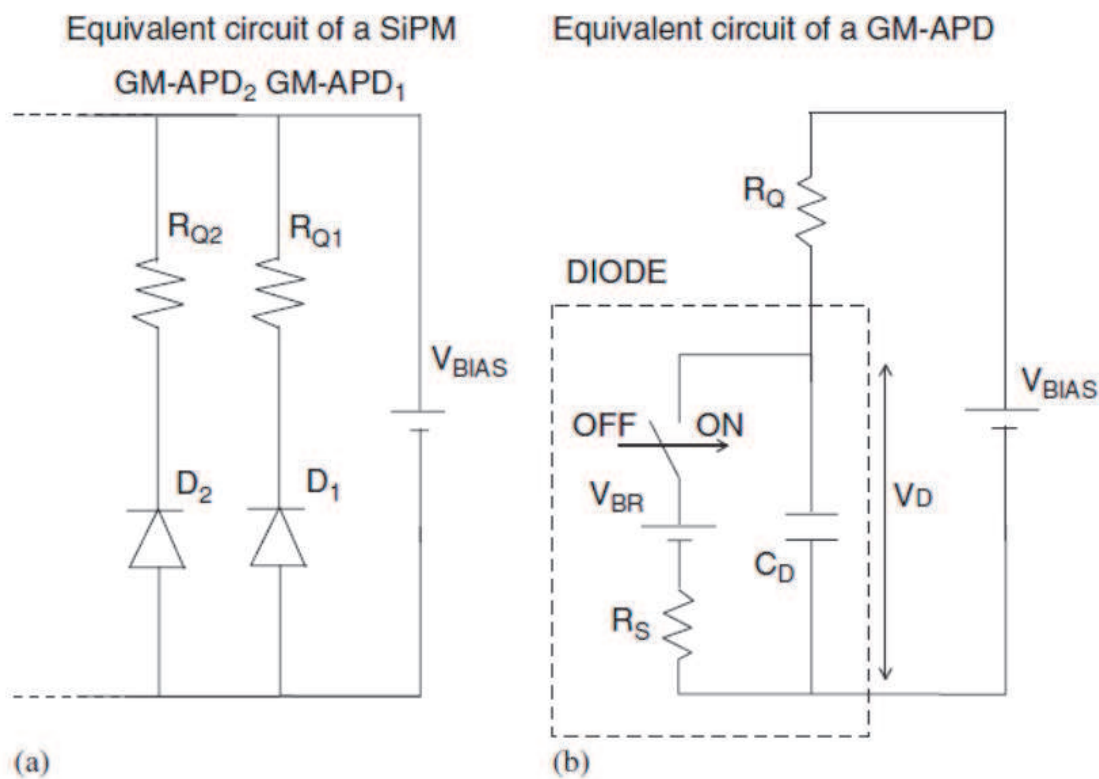


Fig. 11. Equivalent electric scheme of the SiPM

4. Test of static characteristics

The breakdown voltage (V_{break}) and the R_Q values are determined thanks to the reverse and forward current–voltage (I–V) characteristics curves.

The MPPCs used for this work have an active surface of 1 X 1 mm², divided into 1,600 pixels of 25µm x 25µm (Figure 12, Figure 13 and Figure 14), and of 3 X 3 mm², divided in 14,400 pixels of 25µm x 25µm (Figure 15 and Figure 16 : from Hamamatsu data sheet) [34].

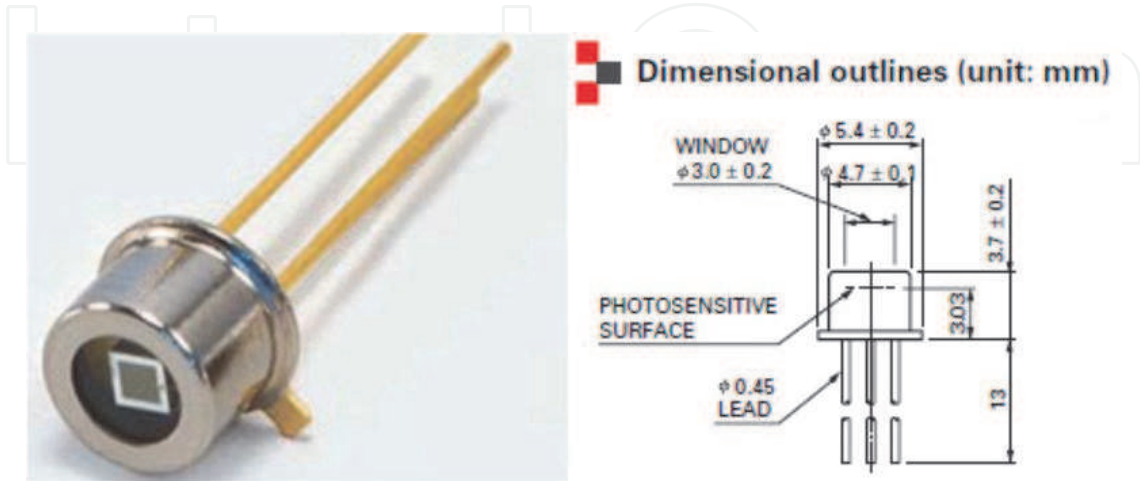


Fig. 12. Aspect and external dimensions of the MPPC 1 X 1 mm² under characterization.

Active area 1 × 1 mm type (Typ. unless otherwise noted, Ta=25 °C)

| Parameter | Symbol | \$10362-11 series | | | Unit |
|--|--------|------------------------|-----------------------|-----------------------|-------|
| | | -025U, -025C | -050U, -050C | -100U, -100C | |
| Chip size | - | 1.5 × 1.5 | | | mm |
| Effective active area | - | 1 × 1 | | | mm |
| Number of pixels | - | 1600 | 400 | 100 | - |
| Pixel size | - | 25 × 25 | 50 × 50 | 100 × 100 | μm |
| Fill factor *1 | - | 30.8 | 61.5 | 78.5 | % |
| Spectral response range | λ | 270 to 900 | | | nm |
| Peak sensitivity wavelength | λp | 400 | | | nm |
| Quantum efficiency (λ=λp) | QE | 70 Min. | | | % |
| Photon detection efficiency *2 (λ=λp) | PDE | 25 | 50 | 65 | % |
| Recommended operating voltage range | - | 70 ± 10 *3 | | | V |
| Dark count | - | 300 | 400 | 600 | kcps |
| Dark count Max. | - | 600 | 800 | 1000 | kcps |
| Terminal capacitance | Ct | 35 | | | pF |
| Time resolution (FWHM) | - | 200 to 300 | | | ps |
| Temperature coefficient of reverse voltage | - | 50 | | | mV/°C |
| Gain | M | 2.75 × 10 ⁵ | 7.5 × 10 ⁵ | 2.4 × 10 ⁶ | - |

Fig. 13. Operating parameters of the MPPC 1 X 1 mm² as delivered by the supplier.

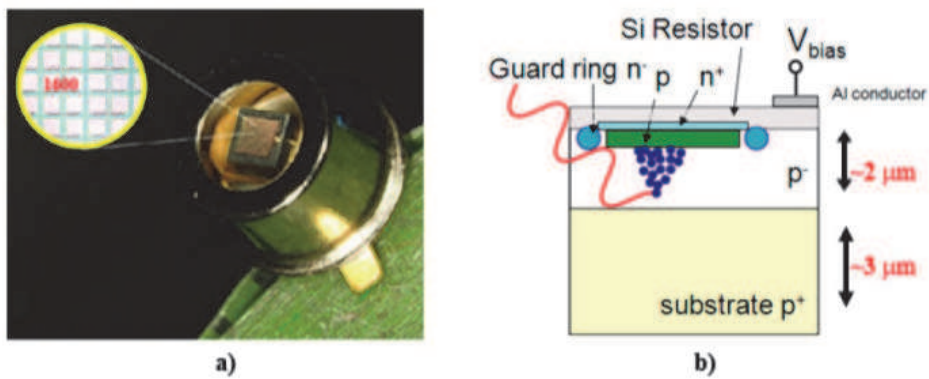


Fig. 14. a) A Photograph of the MPPC S10362-11-025U by Hamamatsu. b) Structure of a MPPC pixel.

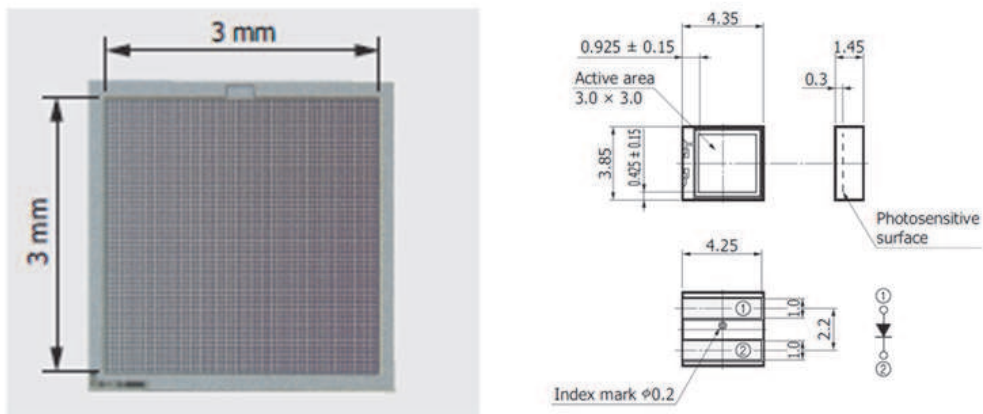


Fig. 15. Aspect and external dimensions of the MPPC 3 X 3 mm² under characterization.

✚ Electrical and optical characteristics (Typ. Ta=25 °C, unless otherwise noted)

| Parameter | Symbol | S10362-33 | | | | S10931 | | | Unit |
|--|--------|------------------------|-----------------------|-----------------------|--|------------------------|-----------------------|-----------------------|-------|
| | | -025C | -050C | -100C | | -025P | -050P | -100P | |
| Fill factor *1 | - | 30.8 | 61.5 | 78.5 | | 30.8 | 61.5 | 78.5 | % |
| Spectral response range | λ | 320 to 900 | | | | 320 to 900 | | | nm |
| Peak sensitivity wavelength | λp | 440 | | | | 440 | | | nm |
| Operating voltage range | - | 70 ± 10 *2 | | | | 70 ± 10 *2 | | | V |
| Dark count *3 | - | 4 | 6 | 8 | | 4 | 6 | 8 | Mcps |
| Dark count Max. *3 | - | 8 | 10 | 12 | | 8 | 10 | 12 | Mcps |
| Terminal capacitance | Ct | 320 | | | | 320 | | | pF |
| Time resolution (FWHM) *4 | - | 500 to 600 | | | | 500 to 600 | | | ps |
| Temperature coefficient of reverse voltage | - | 56 | | | | 56 | | | mV/°C |
| Gain | M | 2,75 × 10 ⁵ | 7,5 × 10 ⁵ | 2,4 × 10 ⁶ | | 2,75 × 10 ⁵ | 7,5 × 10 ⁵ | 2,4 × 10 ⁶ | - |

Fig. 16. Operating parameters of the MPPC 3 X 3 mm2 as delivered by the supplier.

A V_{break} of 70.1 V has been obtained for S10362-11-025U 1 X 1 mm² SiPM, thus demonstrating a good uniformity of the V_{break} for different SiPM's. The value of the quenching resistor extracted from the forward characteristics is of ~145 Ω, giving for a single micro-cell a value of 230 kΩ (see Figure 17). In fact the global resistance measured is related as:

$$R_{SiPM} = R_{micro_cell}/N_{micro_cell}$$

where $N_{micro-cell} = 1,600$ for the S10362-11-025U model of 1 X 1 mm² SiPM and $N_{micro-cell} = 14,400$ for the S10931-025P model of 3 X 3 mm² SiPM.

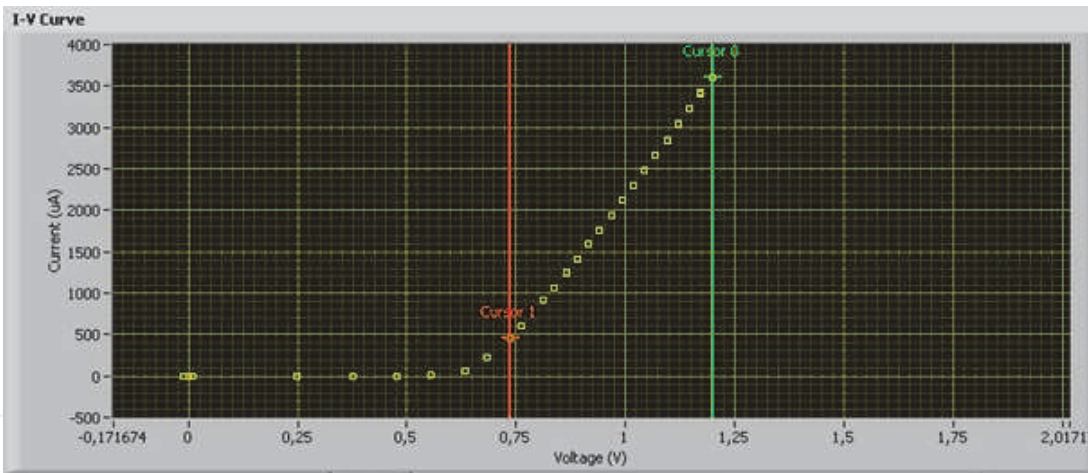


Fig. 17. Forward characteristics of S10362-11-025U SIPM (1 x 1 mm²).

A similar measurement on the 3x3 mm² SiPM led to a global resistance of 26 Ω, giving a single pixel quenching resistance of ~ 380 kΩ. In the Figure 18, the reverse biased portion of the I-V curve is shown, for the 3x3 mm² SiPM. This side of the curve is used to extrapolate from the fit, the most convenient bias voltage to apply to the device.

5. Dynamic characteristic and basic performances

A circuit model, which emulates the evolution of the signal of a GM-APD was developed in the 1960s to describe the behaviour of micro-plasma instability in silicon [35, 36]. According to this model, the pre-breakdown state can be represented as a capacitance (junction capacitance, C_D) in series with the quenching resistor.

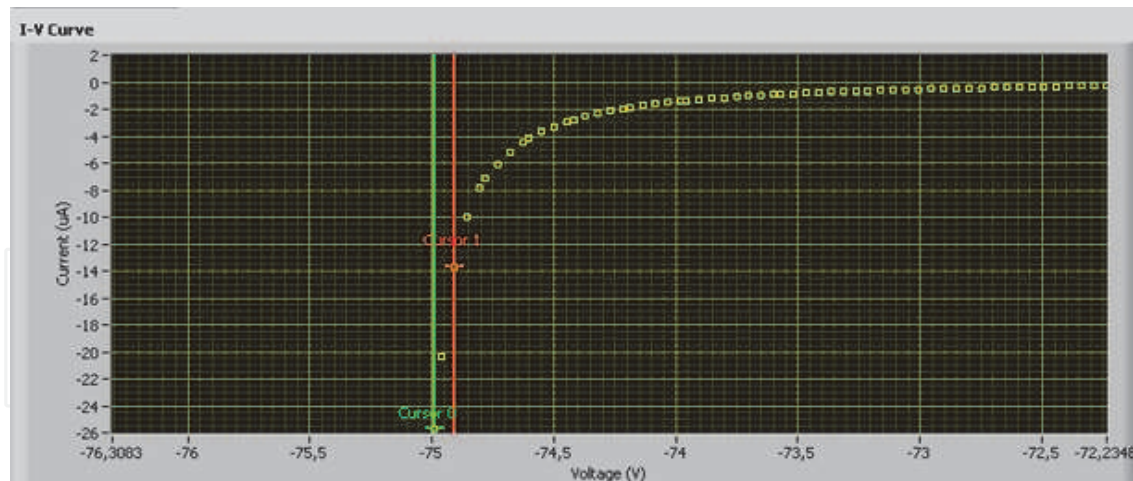


Fig. 18. Reverse side of the Current VS Voltage curve, this time for the 3x3 mm² SiPM.

In steady state, the capacitance is charged at $V_{bias} > V_{break}$. When a carrier traverses the high-field region, (switch closed in Figure 11/b) there is a certain probability, to initiate an avalanche discharge. If this happens, the new state of the system can be modelled adding to the circuit a voltage source V_{break} with a series resistor R_S in parallel to the diode capacitance. R_S ($\approx 1k\Omega$) includes both the resistance of the neutral regions inside the silicon as well as the space charge resistance. C_D , originally charged at $V_{bias} > V_{break}$, discharges through the series resistance down to the breakdown voltage with a time constant τ_D given by the product $R_S C_D$. The discharge current of the avalanche process can take some hundreds of ps. As the voltage on C_D decreases, the current flowing through the quenching resistance tends to the asymptotic value of $(V_{bias} - V_{break}) / (R_Q + R_S)$. In this final phase, if R_Q is high enough (some hundreds of $k\Omega$), the diode current is so low that a statistical fluctuation brings the instantaneous number of carriers flowing through the high-field region to zero, quenching the avalanche.

When the avalanche process is terminated, the switch is again open and the circuit is in its initial configuration with the capacitance charged at V_{break} . At this point it starts recharging to the bias voltage with a time constant $\tau_R = C_D R_Q$ and the device becomes ready to detect the arrival of a new photon (Figure 19). The number of carriers created during an avalanche discharge is given by $n_{carriers} = (V_{bias} - V_{break}) C_D / e$, where e is the electron charge.

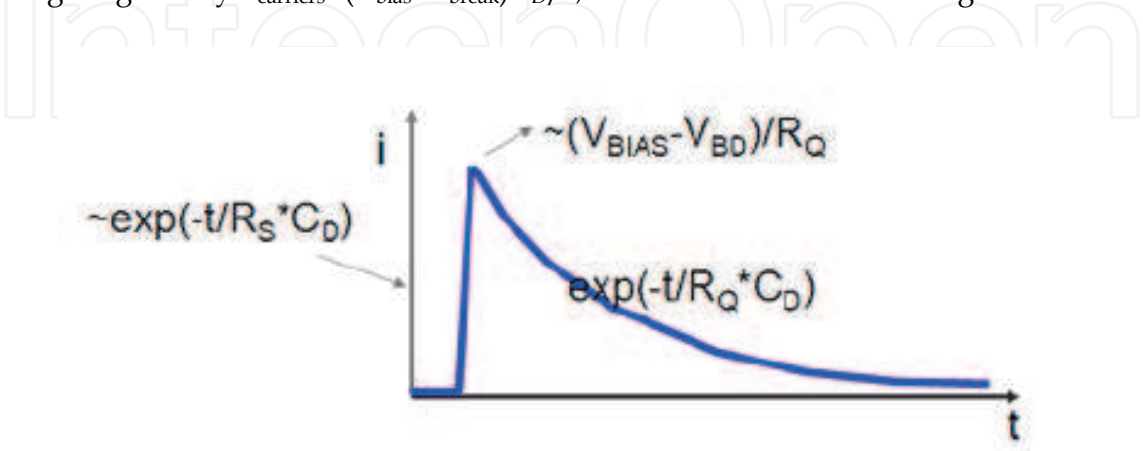


Fig. 19. The time evolution of the current into a cell, when a discharge occurs.

Then the gain of the SiPM (G) is determined by the charge (Q) that can be released from a micro-cell after the breakdown [19]:

$$G = \frac{Q}{e} = \frac{\Delta V C_D}{e} = \frac{1}{e} \frac{\Delta V}{R_Q} R_Q C_D = \frac{I_{\max} \tau_R}{e}$$

where $\Delta V = (V_{\text{bias}} - V_{\text{break}})$ is the overvoltage and $\Delta V / R_Q = I_{\max}$.

The time integration of the micro-cell dark pulse allowed the measurement of the gain. Each diode composing the SiPM reacts independently in the above-described way. Thus, if n cells are activated at the same time, the charge measured at the SiPM output is n times the charge developed by a single GM-APD, giving information on the light intensity.

5.1 Experimental set up

The basic performances of the MPPC's are measured with light from a pulsed laser. All results shown in this section are for a Hamamatsu MPPC of 1x1 mm² and 3x3 mm².

The general scheme of the experimental setup is shown in the Figure 20. The board accommodating the MPPC is placed inside of a dark chamber; the laser, pulsed at a typical frequency of 100 kHz, is connected via optical fiber with a custom connector as coupling device. Two beam splitters are installed along the fiber way in order to reduce the beam intensity and control, for very low intensities, the number of photons: the 1% outputs are used on both splitters, leading to a 10⁻⁴ reduction factor.

The optical power of the installation has been measured using a Newport mod. 815 power meter having a sensitivity of 1 nW obtaining a response of about 50 to 2350 photons per pulse.

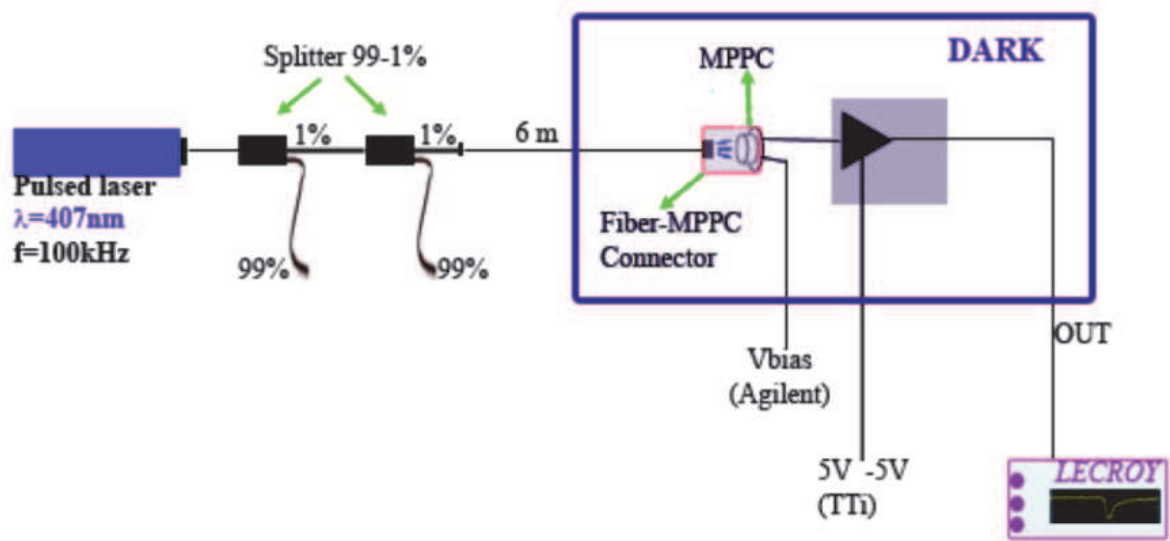


Fig. 20. Scheme of the bench test for the MPPC using laser source and beam splitters.

Figure 21 shows the electric scheme of the board used to amplify the MPPC signals. The detector receives power from a polarization resistor $R_P \sim 10 \text{ k}\Omega$ and its output is connected to the input of a current-to-voltage amplifier. The amplifier is a LMH6624 by National Semiconductor used in inverting configuration and powered by $\pm 5 \text{ V}$. In this configuration

the output of the operational amplifier is directly proportional to the current on the input flowing through the reaction resistance R_f , determining the amplification trans resistance gain and so giving:

$$V_{out} = -i_{in} \cdot R_f$$

(5.1)

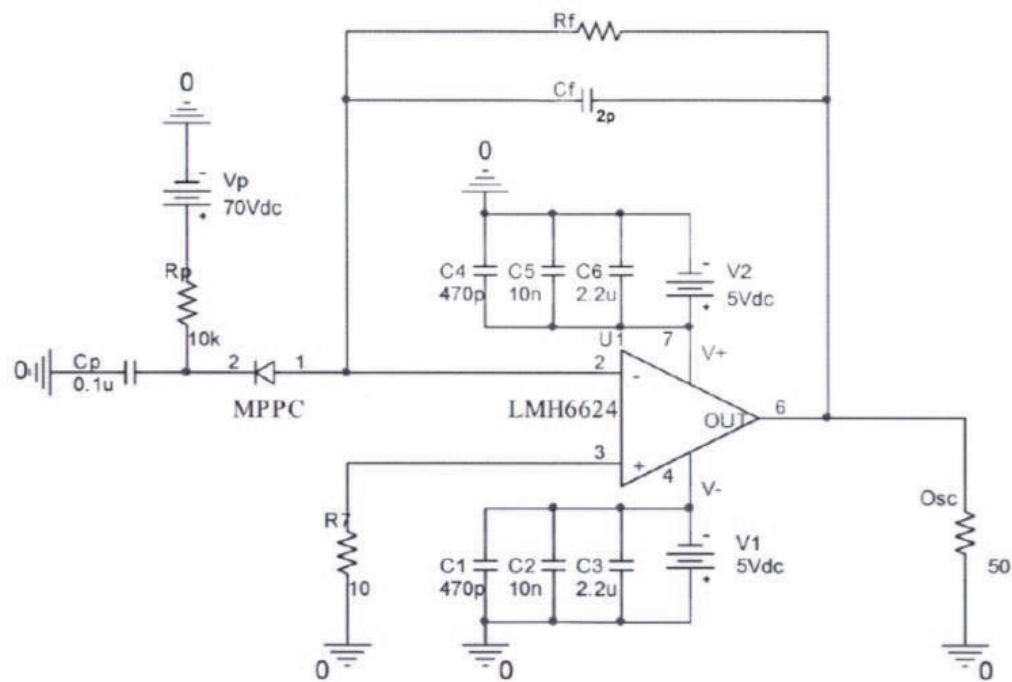


Fig. 21. Schematic diagram of the amplification board designed which accommodates the MPPC.

5.2 Raw signal

Figure 22 shows the raw signal and the output charge spectrum from an MPPC taken with an oscilloscope. The MPPC is illuminated by pulsed light from the laser at low intensity and the oscilloscope is triggered in synch with the laser. The responses for multiple triggers are overlaid in the figure. The charge corresponding to different numbers of fired pixels shows well separated peaks.

This indicates that the gain of each micropixel is uniform, demonstrating the excellent photon counting capability of the MPPC. For bias voltage under 69.8 V on the 1x1 mm² device (and 69.4 V on the 3x3 mm² device) we did not succeeded in observing any signal, since their amplitude is covered by electronic noise. At 69.8 V (69.4 V for the 3x3 mm² device) we observe clear signals of 1 photon equivalent (p.e.) of an amplitude of the order of 2 mV (2.7 mV for the 3x3 mm² device). As the bias voltage increases, higher signals are obtained, so 1 p.e. and signals for 2 or 3 p.e. begin to be always observable. The latter are due to an increased probability of thermally generation and crosstalk events. Around 71.5 V signals for 2 or 3 p.e. become very frequent and it is clear that, in these conditions, it becomes difficult to distinguish between any actual signal and dark count.

Some samples of signal as observed at the oscilloscope at different operating voltages are shown in the Figure 23.

We remark that:

- Rise time and fall time of signals are basically independent from the applied voltage. Rise time is around 1-2 ns; fall time is 2-3 ns and is sensitive to the transition capacitance of the pixels and the quenching resistor, since:

$$\tau_{fall} = (R_P + R_Q) C_D \cong R_Q C_D = \tau_R$$

- Optimal working voltage for this MPPC are around 70.5-71.2 V, values that are compatible with the ones suggested by the manufacturer.

Rise and fall time have been measured at 70.8 V reverse bias, by accumulating 10,000 values and obtaining, for the 1x1 mm²:

$$\tau_{rise} = (1.4 \pm 0.6) \text{ ns}$$

$$\tau_{fall} = (2.0 \pm 0.5) \text{ ns}$$

and 72.1 V reverse bias for the 3x3 mm², obtaining:

$$\tau_{rise} = (8.4 \pm 0.6) \text{ ns}$$

$$\tau_{fall} = (9.9 \pm 0.5) \text{ ns}$$

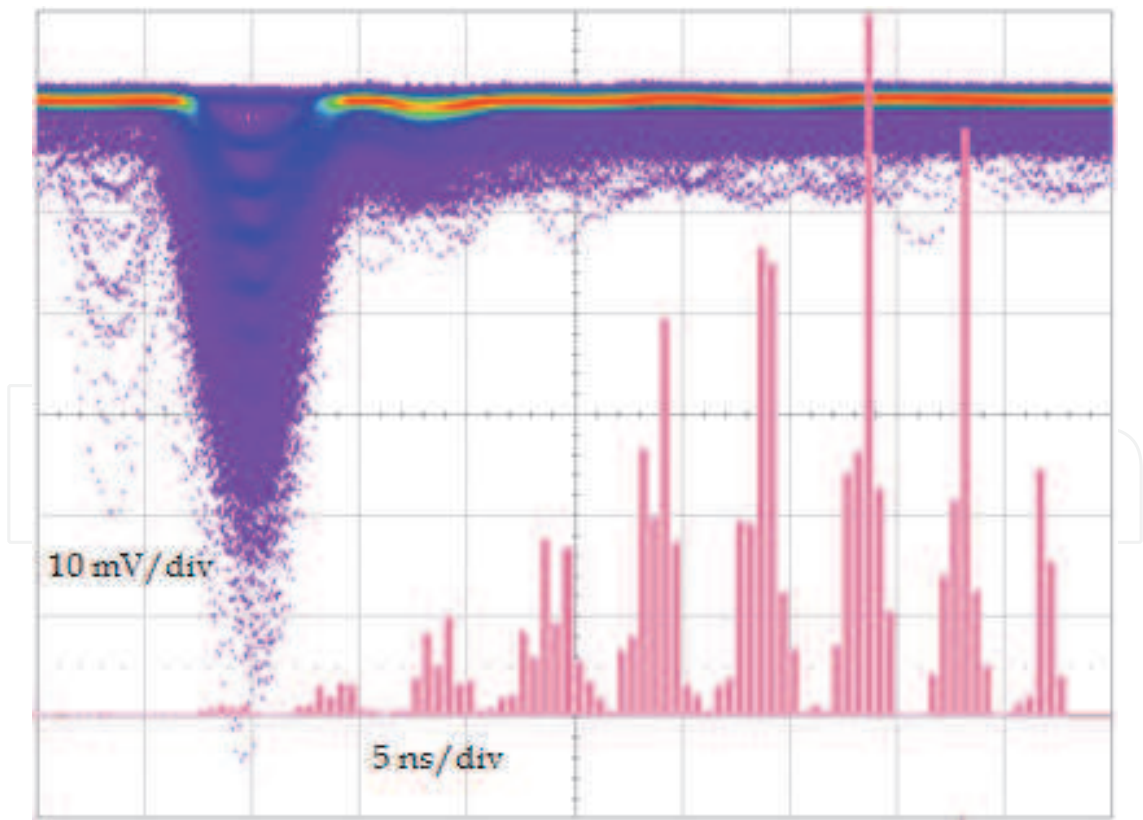


Fig. 22. A collection of pulse signals from MPPC as observed at the oscilloscope for the 3x3 mm² MPPC.

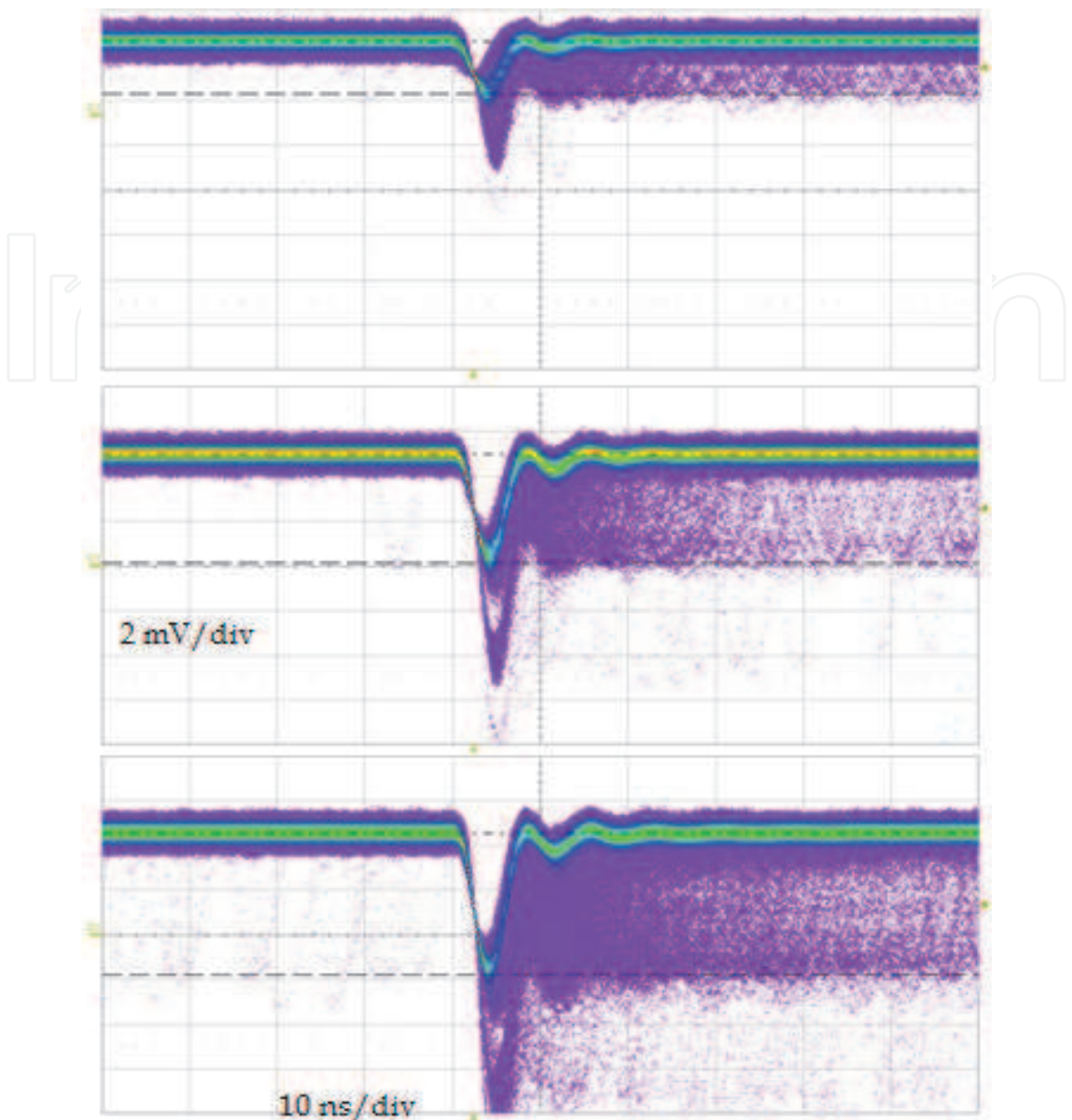


Fig. 23. A collection of pulse signals from MPPC as observed at the oscilloscope for the 1x1 mm² MPPC.

5.3 Gain

From the number of ADC counts between a well-separated pedestal and the peak corresponding to a single fired pixel, we derive the charge corresponding to a it, Q. The gain is defined as Q divided by the charge of an electron:

$$G = \frac{Q}{e}$$

Figure 25 shows the gain measured as a function of the applied voltage for the 1x1 mm² MPPC. The measurement is performed inside a temperature-controlled chamber and data at 22.5 °C are shown. The measured gain depends linearly on the applied voltage as expected. As a second method, the gain can be calculated by measuring the number of channels between two neighboring peaks. To calculate the gain with the second method we put the

MPPC under very low illuminations conditions, allowing to clearly distinguish between peaks of 1, 2, 3 and 4 p.e.. By changing the bias voltage between 71.5 and 74.1 V in 0.2V steps, we measured the difference in the amplitudes of signals of 2 – 1 p.e., 3 – 2p.e. and 4 – 3 p.e.. Figure 22 shows the measurements obtained for 1x1 mm² MPPC whereas histograms on the left in Figure 24 show the results obtained with a 3x3 mm² MPPC. Alternatively, the gain can also be evaluated by measuring the charge of the signal corresponding to the initial number of photoelectrons. The method is shown in the right histogram in the Figure 24, while in Figure 26 the two methods are compared.

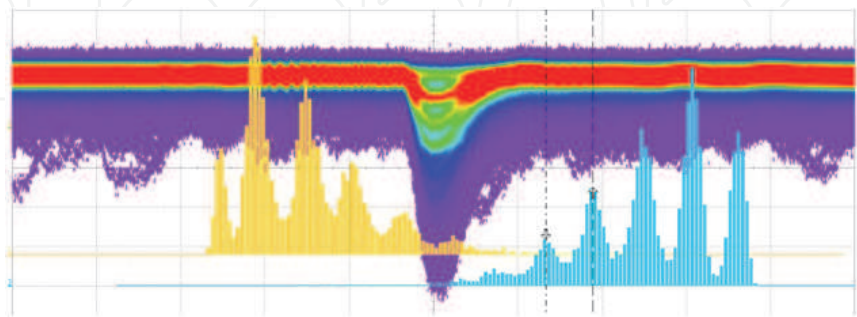


Fig. 24. Pulses from MPPC and gain measurement for the 3x3 mm² MPPC (binning of left histograms is of 5 mV, and ,of right one is 50.0 pVs. Signal shown with 5 mV/div-20ms/div).

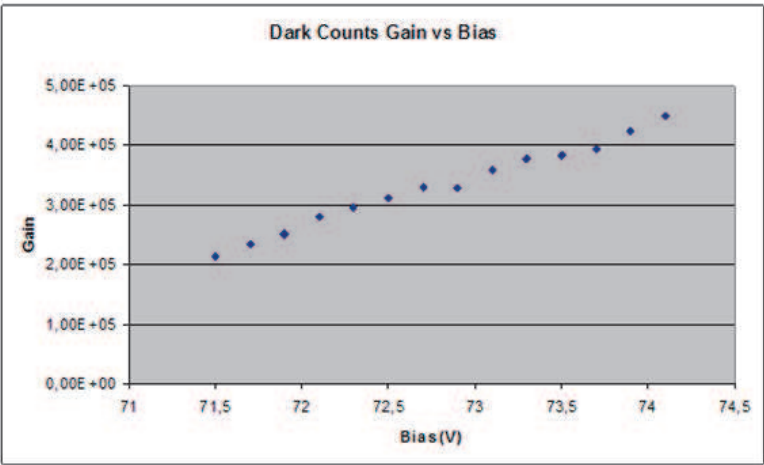


Fig. 25. Measured gain as a function of the applied voltage for the 1x1 mm² MPPC.

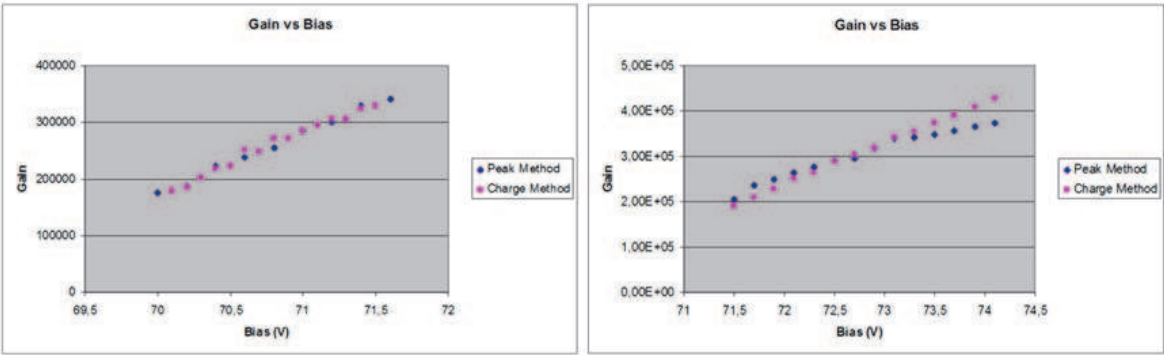


Fig. 26. Comparison between methods for gain evaluation for the 1x1 mm² MPPC (Left) and the for the 3x3 mm² MPPC (Right).

5.4 An estimation of the capacitance

From the gain obtained it is possible to get an estimation of the junction capacitance C_D . In the case of the 3x3 mm² MPPC (1x1 mm² MPPC), from the linear fit of Figure 26, the slope of the fitting line is

$$b = (906 \pm 9) 10^2 V^{-1} \quad ((105 \pm 2) 10^3 V^{-1} \text{ in the } 1 \times 1 \text{ mm}^2 \text{ MPPC})$$

by multiplying this value for the electron charge we get:

$$C_D = (14.51 \pm 0.15) \text{ fF} \quad ((16.74 \pm 0.03) \text{ fF})$$

From this we can get an estimation of the value of the quenching resistor:

$$R_Q = \tau_{\text{fall}}/C_D = (680 \pm 40) \text{ k}\Omega \quad ((119 \pm 30) \text{ k}\Omega)$$

Moreover, since

$$G = \frac{(V_{\text{bias}} - V_{\text{break}})C_D}{e}$$

it is also possible to estimate the breakdown voltage of the device, by extrapolating from the gain line the voltage value corresponding to $G=0$. In the 3x3 mm² MPPC we obtain $V_{\text{break}} = (69.4 \pm 0.7) \text{ V}$, while $V_{\text{break}} = (68.796 \pm 0.005) \text{ V}$ for the 1x1 mm² MPPC.

5.5 Noise considerations

The Geiger-mode micro-cell detection of an event does not give intensity information. The output pulse produced by the detection of a photon is indistinguishable from that produced by the detection of many simultaneously absorbed ones. That means a single thermally generated electron or hole can initiate an avalanche. This gives the main limitation of increasing the sensitive area of Si avalanche structures operated in single photon-counting mode at room temperature. Reduction of the dark counting rate in Si avalanche can be obtained by limiting both the sensitive area (1x1 - 3x3 mm²) and the thickness of depleted region.

Other improvements can be achieved by minimizing the number of generation-recombination centres, the impurities and crystal defect. In addition, the detector operation at low temperature and a good quality in the fabrication process further improve the single photon detection capability. The main effect to be taken into account is the production of after-pulses by charges from the avalanche process that are temporarily trapped, generating a new avalanche after their release (see Figure 27).

After-pulses with short delay contribute little because the cells are not fully recharged, but have an effect on the recovery time. Operation at low temperatures elongate the delayed release by a factor of 3 when the temperature is reduced by 25 °C [21].

Another effect to be taken into account is the optical cross talk due to photon travelling to a neighbouring cell which trigger an avalanche.

In fact, in an avalanche breakdown, there are 1–3 photons emitted in average per carriers, with a photon energy higher than the band gap of silicon. These photons may travel to another pixel of the matrix and initiate an avalanche breakdown there. A dedicated design, with grooves between the cells acting as an optical isolation, reduces the cross talk till two order of magnitude. Operation at a relatively low gain is advantageous in this case.

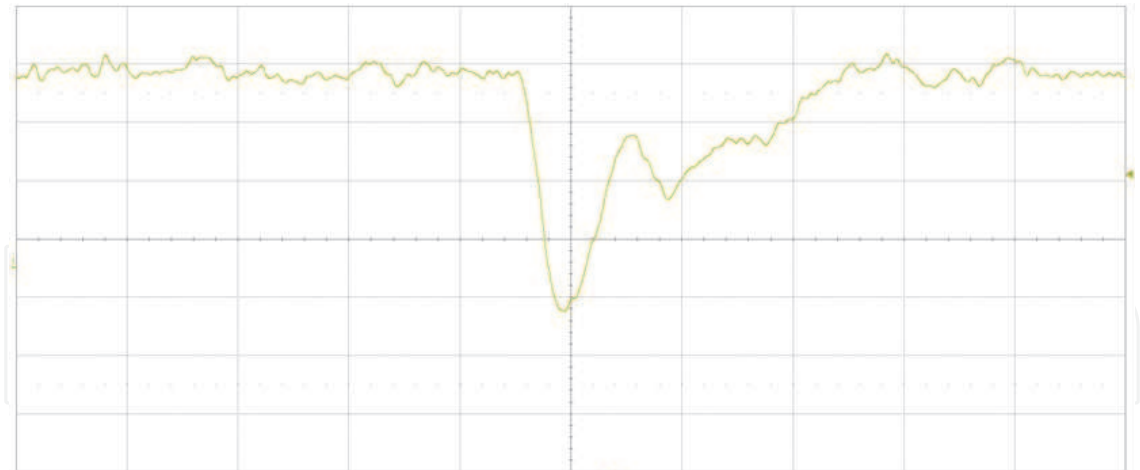


Fig. 27. After pulse event as obtainable at the oscilloscope.

The origin of the cross-talk is presumed to be related to optical photons emitted during avalanche [37] which enter neighboring micro pixels and trigger another Geiger discharge. The probability of causing cross-talk is estimated from the fraction of events with more than one p.e. to that with one p.e. in randomly triggered events without external light. We assume that the events with more than 1 p.e. are caused by the cross-talk from the original Geiger discharge in a single pixel. At low bias voltage, a dark count of 2 p.e. should be related to crosstalk phenomena only because of the low probability that both electrons generate a Geiger discharge. In order to obtain a complete characterization of the device we have measured the dark counts rate as a function of the supply voltage. For every voltage applied we have performed three measures of rate using three different trigger thresholds: 0.5 p.e., 1.5 p.e. and 2.5 p.e. at 23 °C . Results for these measurements are shown in Figure 28. The noise rate decreases as the temperature becomes lower. The temperature coefficient of noise rate at 0.5 p.e. threshold is $-5\text{ \%}/^{\circ}\text{C}$. There is a factor 2 reduction of the dark count every 8°C [21, 38]. These observations imply that the dominant component of the noise is due to the discharge of single pixels induced by thermally generated carriers.

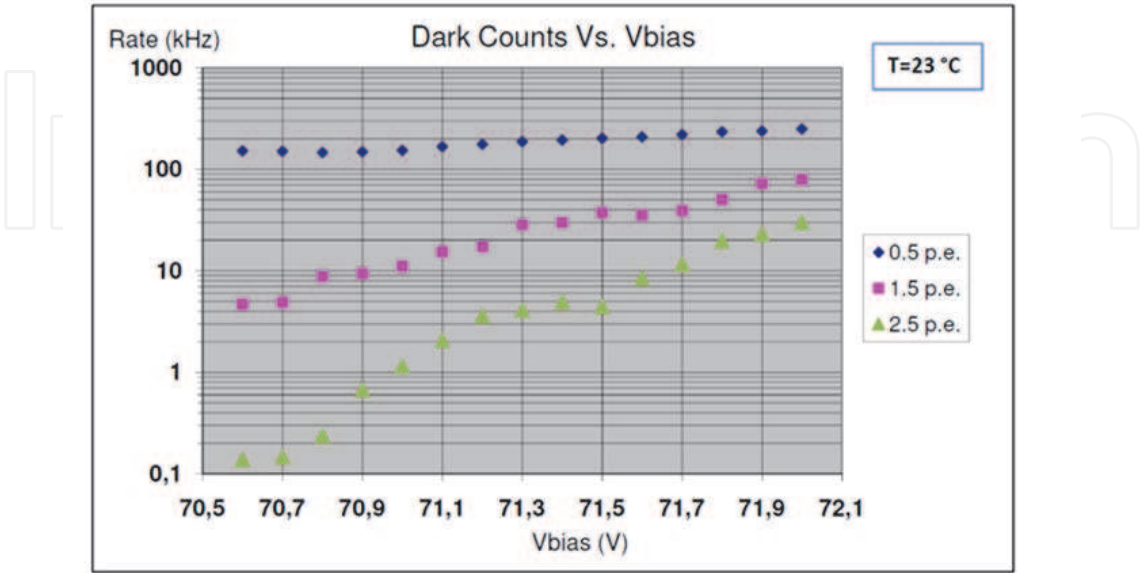


Fig. 28. Dark counts rate generated by the MPPC as a function of the supply voltage.

The measurement of the event rate with 0.5 p.e. trigger gives an estimation of the global noise rate, including the thermal dark counts and the crosstalk events. At 1.5 p.e. of trigger and for low bias voltage, an estimation of the cross talk events only should be possible, since at room temperature we have a low probability that two pixels generate, at the same time, a couple just for thermal excitation.

From the Figure 28 we can remark that the high single rate of the SiPM (if we adopt a low photoelectron threshold) can be easily overcome in those experimental conditions where the time parameter takes a main role. A double coincidence or a gate signal of the right duration can reduce the single rate to acceptable or negligible levels. We have to remind, at this stage of the discussion, that the threshold is of the level of a single or few photoelectrons, a level which would be impossible for classical PMT.

In the following table it is shown the noise rate as a function of the threshold and duration of the coincidence:

| gate duration | Threshold 0.5 p.e | Threshold 1,5 p.e | Threshold 2,5 p.e |
|---------------|-------------------|-------------------|-----------------------|
| 10 ns | 23 Hz | 1 Hz | ~10 ⁻¹⁰ Hz |
| 20 ns | 46 Hz | 0.5 Hz | ~10 ⁻¹⁰ Hz |
| 50 ns | 115 Hz | 0.2 Hz | ~10 ⁻¹⁰ Hz |

These rates are perfectly compatible with the random coincidences rate obtained from the relation $N_1 \times N_2 \times 2T$. Under these conditions we can see that the dark noise is negligible with respect to the collected events. Moreover, even without artifices like the indicated coincidence technique, with a threshold greater than 3 p.e., the single rate becomes acceptable.

6. Detection efficiency for photons and ionizing particles

The efficiency of an SiPM is the product of several factors and depends on the QE, the geometrical efficiency (ϵ_{geom}), the Geiger-triggering probability:

$$PDE = QE(\lambda) \times P_{trigger} \times \epsilon_{geom}$$

The geometrical efficiency ϵ_{geom} represents the fraction of active area in a micropixel. Actually, only part of the area, occupied by the micro-cell, is active and the rest is used for the quenching resistor and other connections (see Figure 29). ϵ_{geom} is defined as the ratio of sensitive to insensitive area, namely the fill factor, and thus depends on the design and layout of the pixels only. It is about 0.3 for a 25 μm pitch sample (as the considered ones) and about 0.7 for a 100 μm pitch sample [34, 39].

The quantum efficiency of the sensitive area is defined by the intrinsic QE of Si (typical QE = 80–90%). The thickness of layers on top of the structure and of the depletion area can be optimized for specific applications. Efficient absorption of photons requires an increase of the thickness in order to maximize photon conversion. On the other side, it is necessary to minimize the depletion area region in order to reduce the dark count rate. Since the QE of the sensitive area is defined by absorption coefficient α in Si, taking into account the probability of reflection of photons on the device surface, photon detection efficiency can be written as:

$$PDE = \epsilon_{geom} (1 - e^{-\alpha x}) P_{trigger} (1 - R)$$

where R is the reflection coefficient and x is the position in which the electron-hole pair is generated. The fraction of the light transmitted to the sensitive volume is conditioned by the topmost layers and the resistive one. For short wavelength in the UV region, the situation is more critical. To improve the sensitivity also in this region it is necessary to optimize the top contact technologie, depletion thickness and n-p configurations. The triggering probability $P_{trigger}$ depends on the position where the primary electron-hole pairs are generated and the over-voltage (ΔV). To enhance the triggering probability, we have to take into account that electrons have in silicon a better chance to trigger a breakdown with respect to holes, by about a factor of 2, and their difference decreases with increasing fields, as shown in Figure 30 [40]. If one electron-hole pair is born at position x , then the probability that neither the electron nor the hole causes an avalanche is given by $(1 - P_e) \cdot (1 - P_h)$ where the function P_e is the probability that an electron starting at position x in the depletion layer will trigger an avalanche and the function P_h is the analogous for holes.

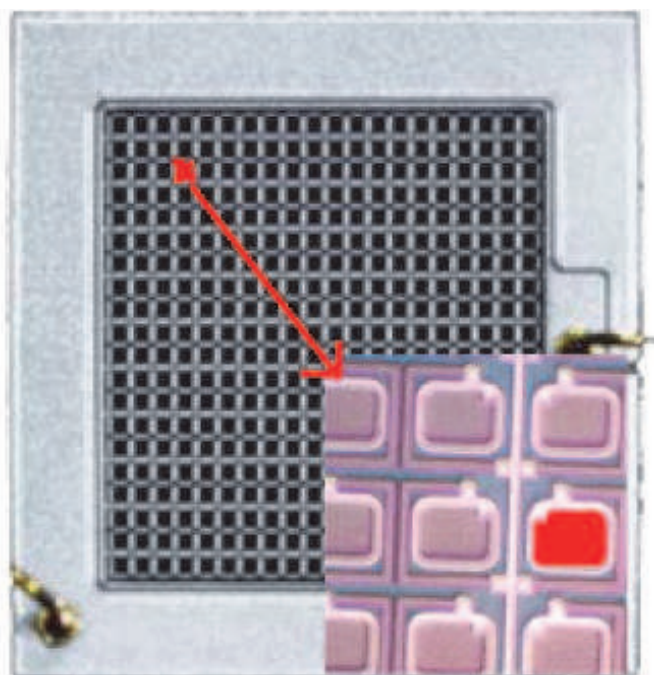


Fig. 29. Matrix of G-APD and evidence of the so called "Fill Factor".

Consequently, the probability $P_{trigger}$ that at x either the electron or the hole initiates an avalanche is given by

$$P_{trigger} = P_e + P_h - P_e P_h$$

Thus, we can write:

$$PDE = \epsilon_{geom} (1 - e^{-\alpha x}) (1 - R) (P_e + P_h - P_e P_h)$$

In case of a photo-generation event, two carriers are created travelling in opposite directions at the absorption point. The contribution to the PDE can be calculated as a function of the generation position by solving two differential equations involving the carrier ionization

rates. If conversion happens in the p depleted region, x is equal to the depleted region thickness (see Figure 2).

In a conventional structure $n^+p\pi p^+$, when a pair is generated in the upper side of the high-field region (n^+), the electron is directly collected at the n^+ terminal (see Figure 31); thus, it does not contribute to the triggering. The hole is forced to pass the whole high-field triggering the avalanche. On the contrary, when the pair is generated in the bottom side (p), the situation is symmetrical and only electrons contribute to the triggering probability. So the triggering probability depends on the position where the primary electron-hole pair is generated and on the overvoltage. A high gain operation is favoured.

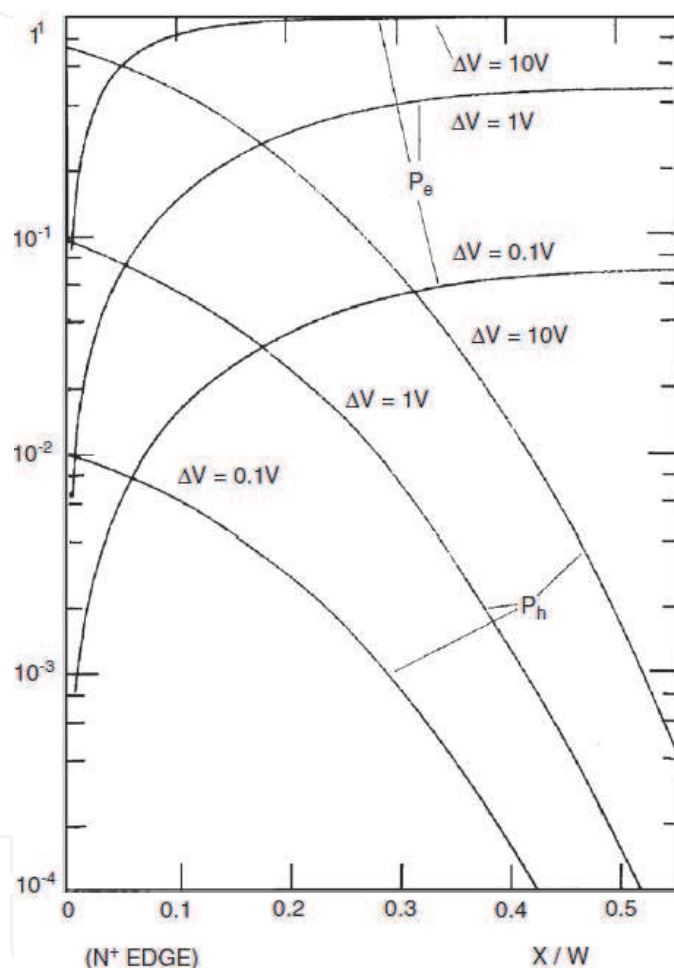


Fig. 30. Avalanche region with width W and the position X which runs from 0 to W starting at the n -edge.

Thus, to maximize the triggering probability, the photon conversion should happen in the p side of the junction, in order to allow the electrons to cross the high-field zone and trigger the avalanche.

As an example for $\lambda > 450$ nm (green and red light) photons convert deep in p -silicon beyond the high-field region. Electrons drift back into the high-field region, triggering avalanches. Hence in this wavelength range the efficiency is very high. For $\lambda < 400$ nm photons are absorbed in the first microns of the n^+ layer. Here the holes drift into the high-field region and trigger the avalanche. Under these conditions the QE is reduced in this wavelengths

range. As a reference for $\lambda = 400$ nm (corresponding to photon energy = 3.10 eV) the absorption coefficient is $1.2 \times 10^5 \text{ cm}^{-1}$ and the thickness required to absorb more than 99% of the light is $\sim 1 \mu\text{m}$ (see Figure 5, where the absorption length as a function of the wavelength is shown) [41-43]. Several solutions exist for increasing the sensitivity at short wavelengths:

- an higher reverse bias voltage would increase the avalanche probability for holes, though the voltage has to be limited due to the increase of cross talk and dark rate
- entrance windows has to be made as thin as possible [44, 45]
- the n^+ layer has to be as shallow as possible (for optimum QE); with standard equipment for detector fabrication, layers with a junction depth of 100 nm can be obtained. The high-field region should be as thin as possible in order to convert photos beyond it.
- Triggering probability can be improved by maintaining the same doping profile configuration but reversing the types, i.e. having a $p^+ - n - n^+$ structure, and making the junction deeper ($> 0.4 \mu\text{m}$). Hence the roles of electrons and holes are reversed, resulting in avalanches triggered by electrons at short wavelengths (Figure 31).

In conclusion, to maximize the triggering probability: (i) the photo generation should happen in the p side of the junction in order for the electrons to pass the whole high field zone, and (ii) the bias voltage (V_{bias}) should be as high as possible.

A better scenario is obtained when electron bombardment is considered. In Figure 32 a simulation for the range of electrons penetrating into the silicon is shown. The simulation has been computed by using Geant4 Simulation Toolkit [46, 47]. If ionizing particles, like electrons, are detected in a n^+pp^+ junction, the range - i.e. the energy - will determine where the carriers are generated. If the end of range is in the p region beyond the high-field area, both carriers created along the track will be travelling in the opposite directions, contributing to the avalanche-triggering probability. Electrons detection efficiency can be evaluated from the following:

$$EDE = \varepsilon_{\text{geom}}(1 - R_{\text{back}})P_{\text{trigger}} = \varepsilon_{\text{geom}}(1 - R_{\text{back}})(P_e + P_h - P_eP_h)$$

where P_e and P_h are the electron and hole breakdown initiation probabilities and R_{back} is the backscattering probability. When a pair is generated before the high field region, the electron is collected at the n^+ terminal; thus, it does not contribute to the trigger. The hole is forced to pass through the full high-field region and so its triggering probability is given by P_h . For pairs generated beyond the high field region, the situation is reversed and only electrons contribute to the triggering probability P_e . These probabilities depend on the impact ionization rates of holes and electrons, respectively. As pointed out above, the electron has an ionization rate of about a factor 2 higher than the hole.

The reduction of the thickness in n^+ layer allows lowering the detectable electron energy. As an alternative, maintaining the same doping profile configuration but reversing the types, i.e. using a p^+nn^+ structure and making the junction deeper, can improve the triggering probability. In this case the electron range is completely contained inside the p^+ region.

6.1 Dynamic range

SiPMs produce a standard signal when any of the cells goes to breakdown. When many cells are fired at the same time, the output is the sum of the standard pulses. Single photons produce a signal of several millivolts on a 50Ω load. For a matrix of $N_{\text{microcells}}$ microcells, the dynamic range is limited by the condition that $(N_{\text{ph}} \times \text{PDE} / N_{\text{microcells}}) < 1$, where N_{ph} is the number of photons, and PDE the Photon Detection Efficiency of the SiPM.

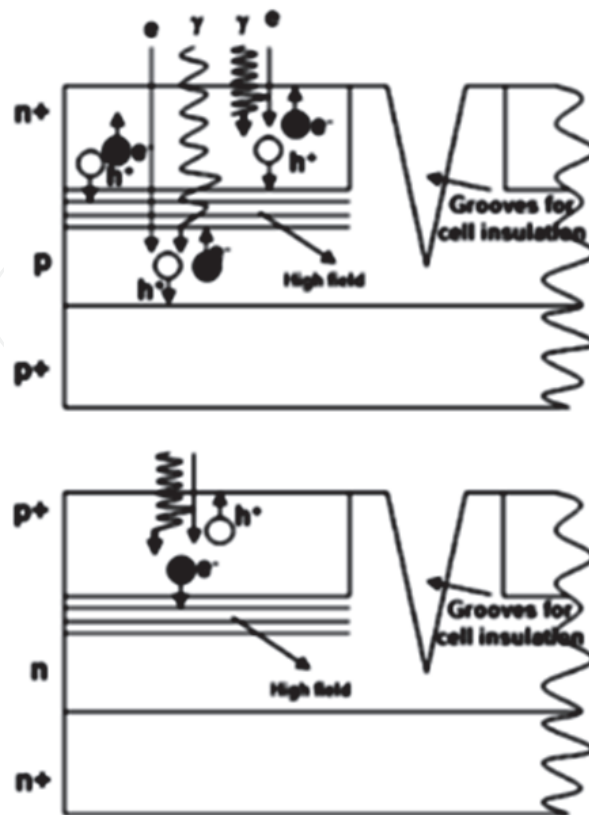


Fig. 31. Photon and electron avalanche induced in the two silicon configurations (p^+nn^+ and n^+pp^+).

In other words, the average number of photons per cell should be less than 1. If the number of detected photons is much smaller than the number of cells, the signal is fairly linear and saturates when the number of photons is about equal to the number of cells. Saturation is well described by:

$$N_{\text{signal}} = N_{\text{microcells}} \times \left[1 - \exp\left(\frac{-N_{\text{ph}} \times PDE}{N_{\text{microcells}}}\right) \right]$$

6.2 Timing

The active layers of silicon are very thin (2–4 mm), the avalanche breakdown process is fast and the signal amplitude is big. Therefore, very good timing properties even for single photons can be expected. Fluctuations in the avalanche development are mainly due to a lateral spreading by diffusion and by the photons emitted in the avalanche [48, 49]. As shown in Figure 34 for the case of $1 \times 1 \text{ mm}^2$ MPPC, operation at high overvoltage (high gain) improves the time resolution.

The dependence of the FWHM as a function of the number of photoelectrons as shown in Figure 35 is in fair agreement with Poisson statistics. The resolution with 15 photo-electrons, typical of applications where SiPM are coupled to small volume, high light yield scintillators, is better than 25 ps.

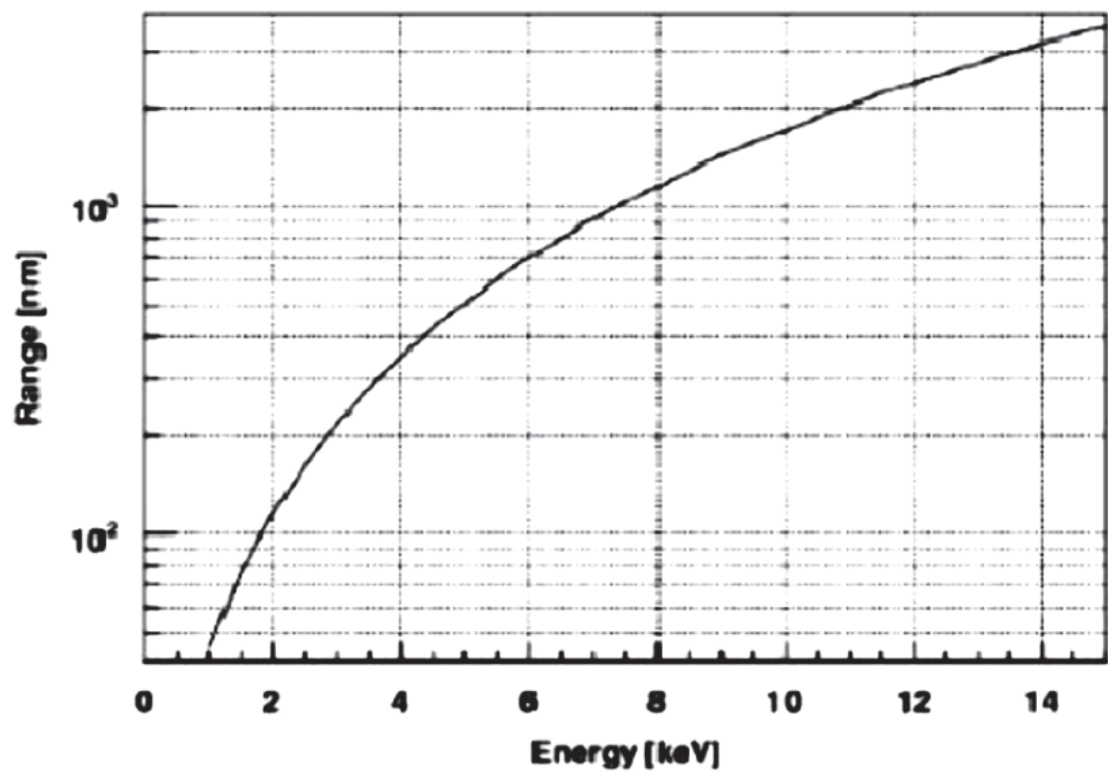


Fig. 32. The range of electrons in Silicon as obtained from a GEANT4-based simulation.

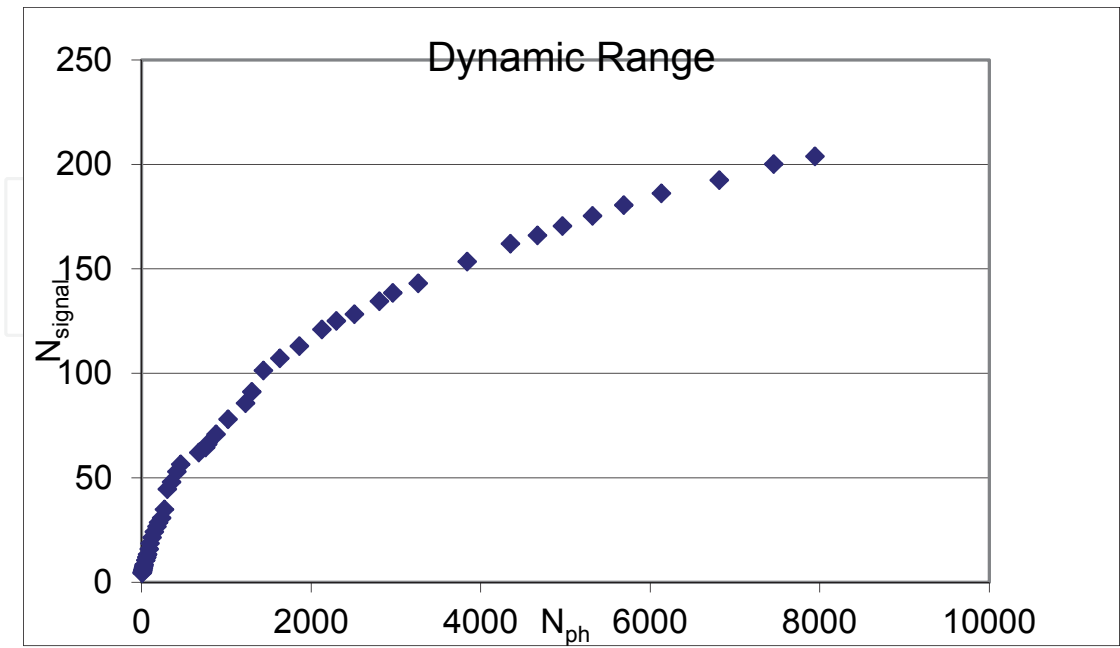


Fig. 33. Dynamic range

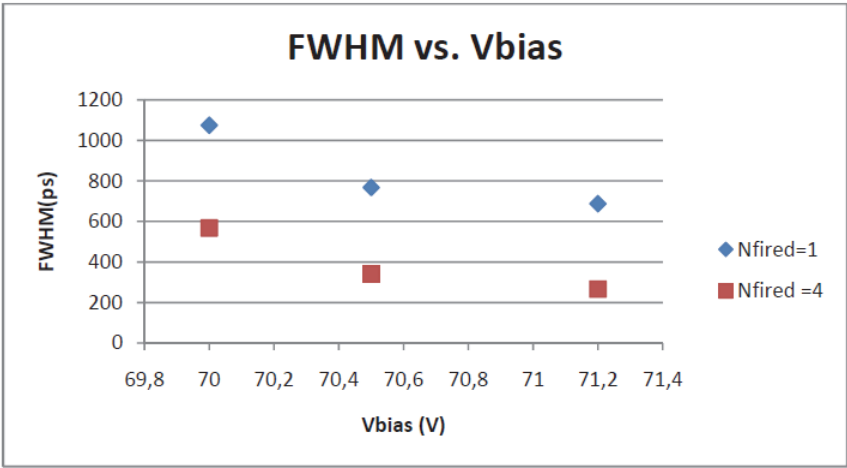


Fig. 34. Time resolution for 1 and 4 photons for the 1x1 mm² MPPC as a function of V_{bias} .

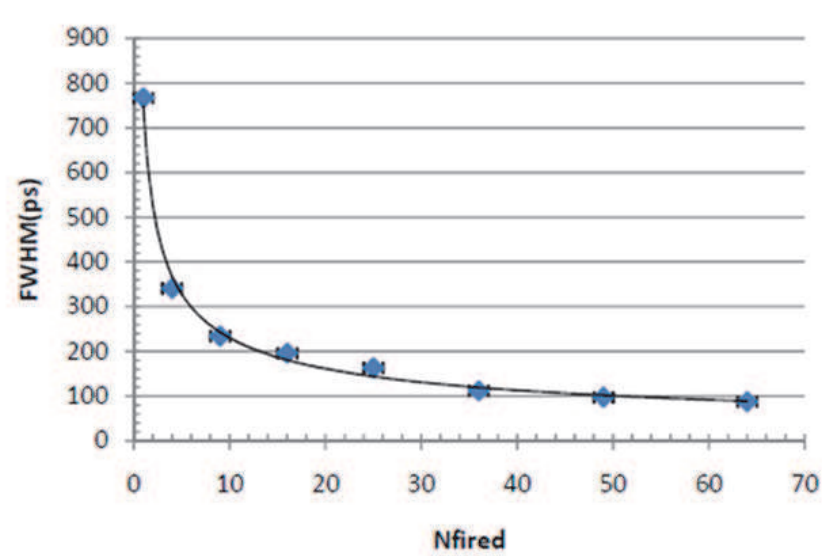


Fig. 35. Time resolution as a function of the number of fired pixels

7. New concepts for semiconductor photomultiplier

The present commercial production of avalanche Geiger-mode photodiodes gives the starting point for a new photomultiplier age, based on p–n semiconductors. As an example, in the Hamamatsu production at least three types of n⁺pp⁺ Multi-Pixel Photon Counter (MPPC) exist: 1600 (25μm×25μm), 400 (50μm×50μm) and 100 (100μm×100μm) pixels segmented onto a 1x1-mm² total active area. The achieved gain, 10⁵–10⁶ at 70–72 V reverse bias voltage, makes possible the one photon level detection. The dark count rate is suppressed to a few hundreds kHz level, by setting a threshold at 0.5 p.e.. It decreases to 1 kHz for 1.5 p.e. and it is not significant for 2–3 p.e. Thermally generated free carriers can be further reduced by cooling the device. The temperature coefficient of noise rate at 0.5 p.e. threshold is -5%/°C. With the present structures the most sensitive wavelength region is around 400 nm where the PDE is 25% for the 1600 pixels type, 50% for the 400 pixels type and 65% for the 100 pixels type [34], reflecting the higher geometric factor value.

At present, the silicon wafer cost and the thermal dark current limit the dimensions of the SiPM photodetector at a few mm².

Now the question is how to detect photons from large surfaces and/or volumes.

Their transport and/or focusing from surface and volume can be achieved in three different ways:

1. collecting photons and conveying them towards a single SiPM device;
2. enlarging the sensitive detector area by ordering several SiPMs in a pixelated matrix shape or by focusing the light to the sensitive area by Winston cones, pyramidal waveguides or lenses
3. making a photon conversion by a vacuum hemispherical photocathode which focuses photoelectrons on a SiPM (VSiPMT).

7.1 SiPM coupled to WLS fibers

The reduction of geometrical area can be obtained by using wavelength shifter fibres embedded in the plastic scintillator body and connected at the other end to the SiPM.

Light collection from large scintillators or complex geometries can sometimes be aided through the use of optical elements that employ wavelength shifting technique. Many liquid or plastic scintillators incorporate an organic additive whose function is to absorb the primary scintillation light and reradiate the energy at a longer wavelength. It is emitted isotropically uncorrelated respect to the direction of absorbed light.

The same light collection principle can be applied using plastic fibers whose contains a wavelength medium. For best light propagation along the fiber one want a large shift between the optical absorption and the emission band so that minimal self-absorption takes place.

One of the first experience in this technique has been achieved in T2K experiment with the usage of wavelength shifter fibers. In this application [50], the counters are readout via WLS fibers embedded into S-shaped grooves in the scintillator from both ends by multi-pixel avalanche photodiodes operating in a limited Geiger mode. A customized 667-pixel MPPC was developed for T2K by Hamamatsu Photonics [51] with a sensitive area of 1.3×1.3 mm² and a pixel size of 50×50 μm²; the sensitive area is larger than those available previously and relaxes the mechanical tolerances required for coupling to the WLS fibers used extensively in the experiment.

7.2 Compound Parabolic Concentrators (CPC)

Image compression from large-surface detectors can be realized using matrices of single SiPM pixels. Such a device is particularly suitable in experiments detecting the Cherenkov or fluorescence light in the atmosphere. A light concentrator can be used to enhance the number of incident photons on the sensitive surface of the detector.

Some experiment for VHE gamma-ray astronomy (as example VERITAS [52], MAGIC [53] and HESS [54]) already use non-imaging light collectors to concentrate light on photomultiplier tubes, while light concentrators are also widely used in diverse fields, as solar energy production.

Compound Parabolic Concentrators (CPC), also known as Winston cones [55], are light-collection devices intended to concentrate light on a smaller area by maximizing photon density per unit surface. Characteristic parameters for CPCs are: dimensional geometry, compression, acceptance angle and collection efficiency. CPCs are usually produced with amorphous (vitreous) materials like commercially available B270 and BK7.

A three-dimensional compound parabolic concentrator is designed by rotating a parabola around the optical axis. The analytical description of the CPC profile is given by the following equation [55]:

$$(r \cos \theta_{\max} + z \sin \theta_{\max})^2 + 2a'(1 + \sin \theta_{\max})^2 r - 2a' \cos \theta_{\max} (2 + \sin \theta_{\max})^2 z - a'^2(1 + \sin \theta_{\max})(3 + \sin \theta_{\max}) = 0$$

in which θ_{\max} is the acceptance angle and a' the exit aperture radius. r and z are, instead, the reference axes as shown in Figure 36.

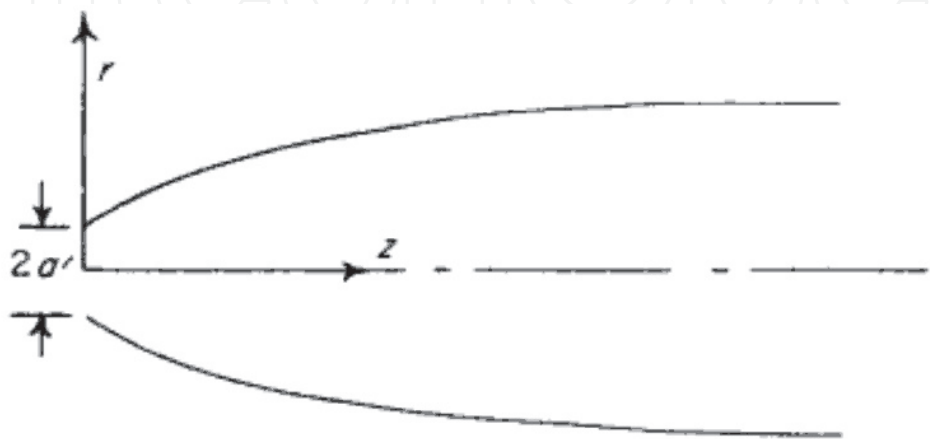


Fig. 36. CPC Profile

As shown in Figure 37 a Winston cone is a double paraboloid built from two off axis parabolas, such that the focal point of one falls to the edge of another. The reflecting surface is obtained by rotating the parabola around the concentrator axis.

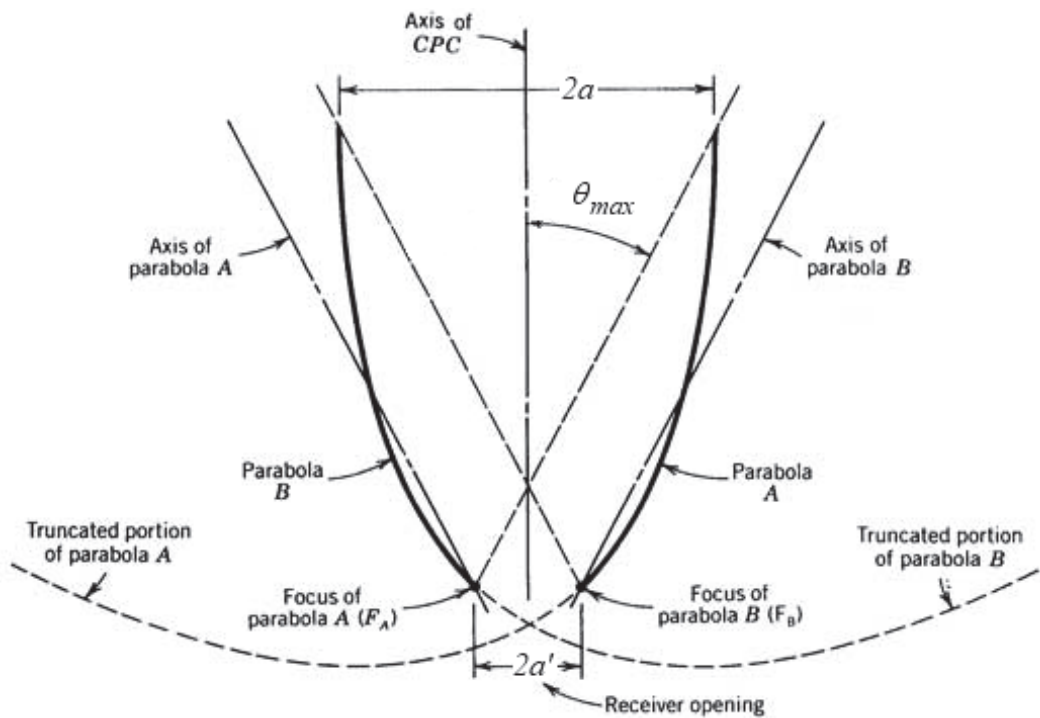


Fig. 37. CPC profile and acceptance angle (θ_{\max}).

The overall length of the parabolic concentrator is conditioned by the symmetry that must ensure to pass both edging rays and is thus limited by the maximum entrance diameter. The overall length is given by:

$$L = \frac{a' (1 + \sin \theta_{\max}) \cos \theta_{\max}}{\sin^2 \theta_{\max}}$$

Since the diameter of entrance surface is:

$$a = \frac{a'}{\sin \theta_{\max}}$$

resulting:

$$L = (a + a') \cot \theta_{\max}$$

A useful ratio for describing the characteristics of a concentrator is the geometrical concentration ratio or compression [55] defined as:

$$C = \text{entrance surface} / \text{exit surface}$$

The theoretical maximum concentration ratio for a three-dimensional design is thus given by:

$$C_{\max} = \frac{a^2}{a'^2} = \frac{1}{\sin^2 \theta_{\max}}$$

where θ_{\max} is the acceptance angle. The acceptance angle (or the cut-off angle) is the angle beyond which most of the light entering the concentrator is reflected out of it: the rays inside the collector undergo multiple reflections, and some of the rays that enter at angles smaller than the limit value can be turned back; some rays incident at angles larger than the limit angle are instead transmitted.

The optical concentration ratio, considering losses (the optical efficiency), is the amount of emerging light at the exit aperture compared to the amount of the incident light on the entrance aperture. The attenuation in the concentrator results from reflection losses, scattering and absorption. Light collection efficiency depends on the radiation incident angle (relative to the Winston cone symmetry axis) and on the acceptance angle. In particular, the efficiency drops as large as the acceptance angle.

Thus, defining the transmission efficiency ϵ_{trans} as:

$$\epsilon_{\text{trans}} = n_d / N_{\text{phot}}$$

where n_d is the number of photons reaching the exit aperture and N_{phot} is the total number of photons penetrating the entrance aperture, the collection efficiency (ϵ_{coll}) can be written as:

$$\epsilon_{\text{coll}} = \epsilon_{\text{trans}} \cdot C_{\max}$$

The collection efficiency is strictly related to the number of multiple reflections before reaching the exit aperture.

Even if the CPC have been designed for solar energy applications, their utilization in low photon detection is attractive to extend the detection surface. In this case, also the impact point

on entrance surface has to be taken into account since this leads to a non homogeneous efficiency. As we will show, better results are obtained with acceptance angles lower than 5° . As shown in Figure 38/left (related to a cone with an acceptance angle of 10° and 8° incident photons), it's possible to identify areas on the entrance surface for which the number of multiple reflections is almost the same.

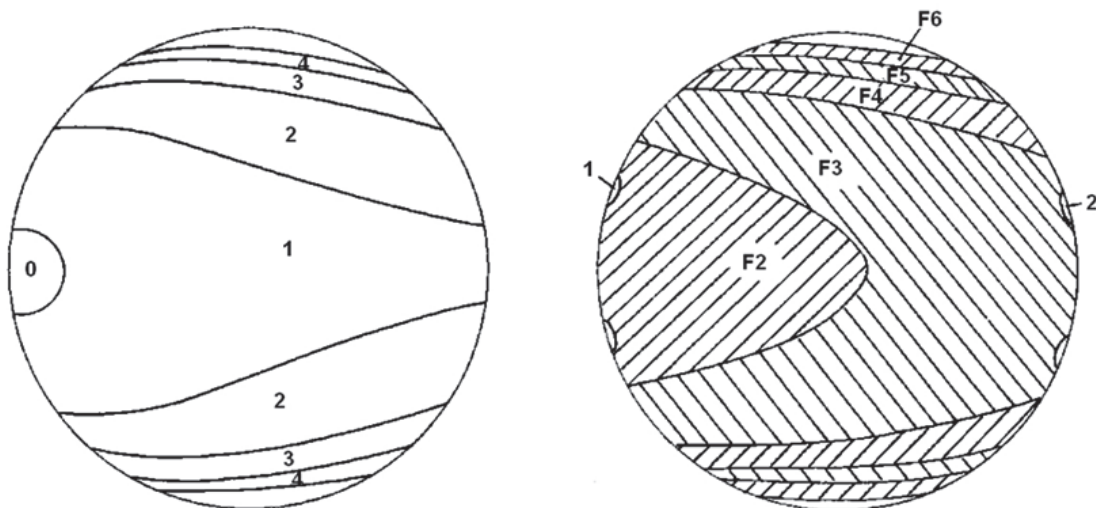


Fig. 38. Left: Transmission zones of rays on the entrance surface of a CPC having $\theta_{\max} = 10^\circ$ for impinging photons at 8° ; Right: Rejections zones of rays on the entrance surface of a CPC having a θ_{\max} of 10° , for impinging photons at 11.5° : remark in (1) two little zones where the transmission is preserved.

Likewise, it's possible to identify the areas where the photons exit from the entrance surface after reflections inside the CPC, without reaching the exit surface. These areas are shown in the Figure 38/right, for an 11.5° incident photons.

In order to estimate the collection efficiency of the light concentrator and to study its dependence on the length of the funnels and on the angle of incidence, we carried out several Monte Carlo simulations. Photons with given direction were produced at the entrance aperture and their path was followed until they were either absorbed by the funnel walls or left the funnel through one of the apertures. Various types of paraboloids and pyramidal light concentrators were examined in the simulations.

Figure 39 shows a Winston cone simulated with a 0° acceptance angle with an entrance and exit apertures of a radius of 28 mm and 5.5 mm, respectively, corresponding to a concentration ratio of 25.91.

The transmission and collection efficiency for this device as a function of photon incident angle (with an uniform distribution of photon impact point) is shown in Figure 40.

As shown in Figure 40, the transmission efficiency, evaluated as n_d/N_{phot} , is strongly suppressed for non-perpendicular photon incident angles, in the case of devices designed with a 0° acceptance angle. However, the efficiency is about 50% for 10° incident angles.

The collection efficiency takes into account also the compression ratio ($\epsilon_{\text{coll}} = \epsilon_{\text{trans}} \cdot C_{\max}$); simulation shows that, at an incidence angle of about 20° , the collection efficiency is 1: the density of photons on the entrance surface is the same of that on the exit surface and the concentrator is useless.

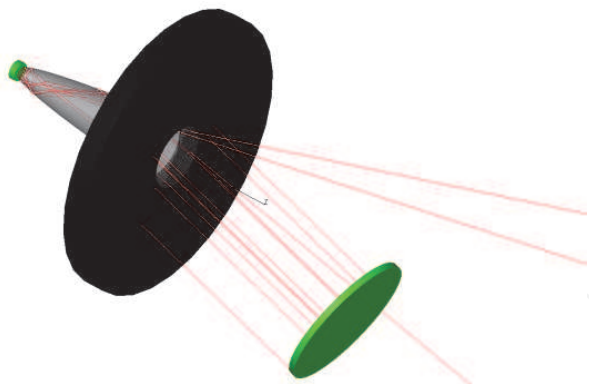


Fig. 39. 3-D model of the CPC with an acceptance angle of 0° used for the simulation.

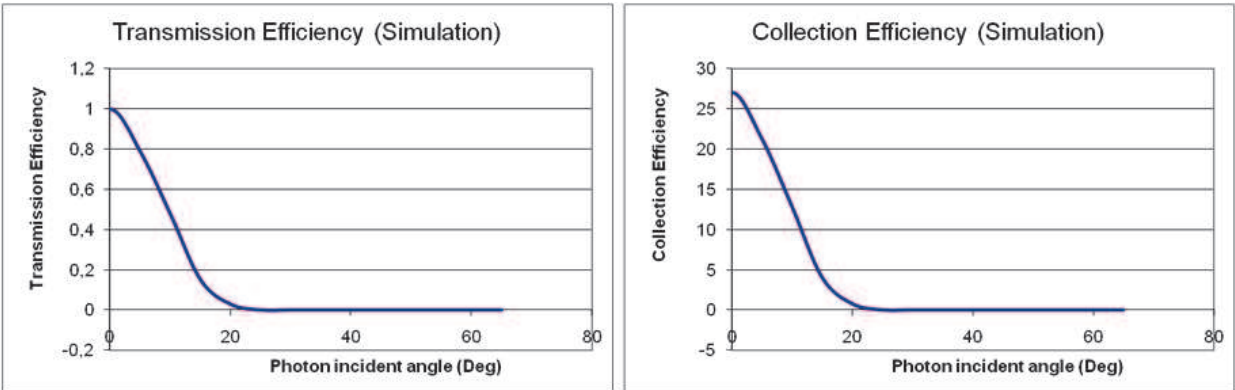


Fig. 40. Simulated transmission (left) and collection efficiency as a function of incident photon angle.

It makes sense the use of a CPC to increase the detection surface of a silicon device only if the devices have a large acceptance angles. To explore this option, a detailed simulation of a CPC with 25° acceptance angle (CPC_{25°) has been performed. CPC_{25° is an optical glass B270 cone having 9.01 mm entrance diameter, 2.50 mm exit diameter, and is 19.25 mm long, commercially available by Edmund Optics [56]. Figure 41/left shows the tridimensional model used in the simulations while Figure 41/right shows the CPC_{25° used for the measurements.

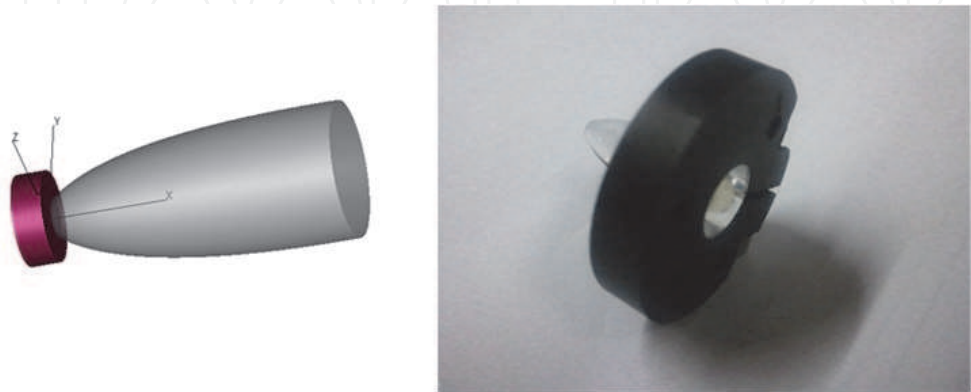


Fig. 41. Left: 3-D model of the CPC_{25° having an acceptance angle of 25°. Right: A photography of the CPC cone used for measurements mounted on its support.

Simulations show that the concentrator is able to transmit photons with incident angle up to about 25° with a good collection efficiency, ranging between 0.5 and 0.8 depending on the incident angle. A small lack in the transmission efficiency is evidenced for 0° incident photons, with respect to the case of a 0° acceptance angle designed one.

In order to experimentally check for the simulation accuracy, we used two different settings. The first set up is shown in Figure 42.

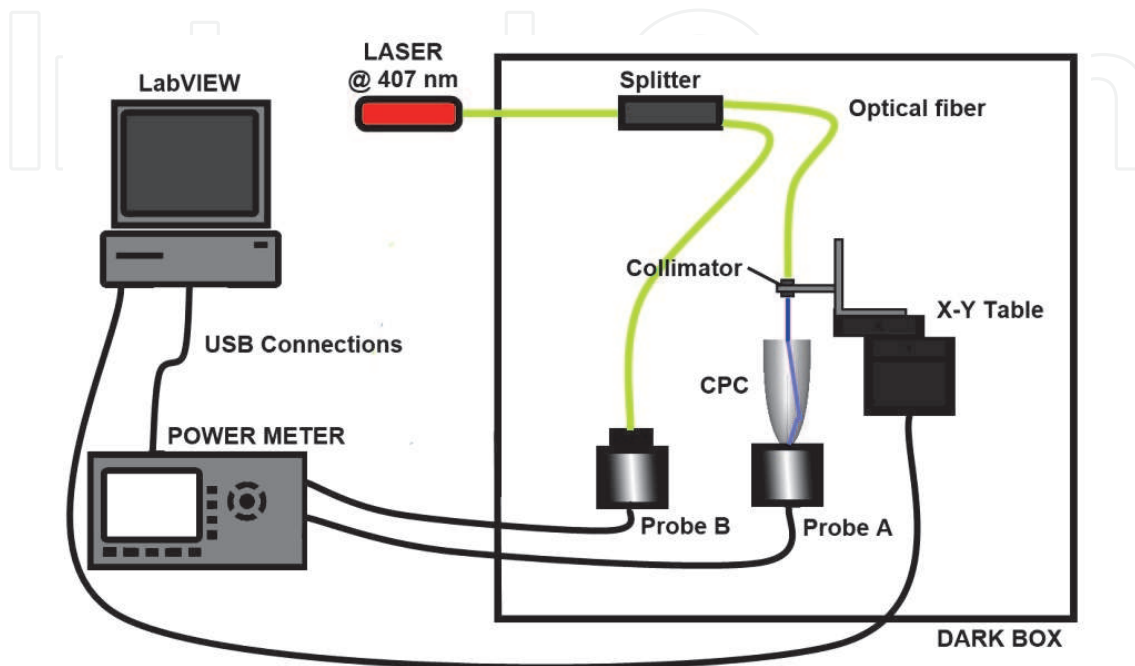


Fig. 42. The experimental setup.

The efficiency of a CPC_{25° has been measured as a function of the impact position on the concentrator entrance surface by employing a computer controlled x-y movement with a position precision of tens of microns. A $\lambda=407\text{ nm}$ highly collimated pulsed laser beam (spot diameter = 0.9 mm) has been sent on the CPC_{25° and both beams at the entrance and exit surfaces have been measured by a double channel Power Meter Newport mod. 2936-C.

The intrinsic efficiency measured is strongly dependent on the impact point of the photon on the entrance surface, as shown in Figure 43.

The measurements of the transmission efficiency along the CPC_{25° diameter, superimposed to the simulation results, are shown in Figure 44 for impinging photons at 0° and at 20° : the simulation correctly reproduces the measurements and confirms the efficiency dependence on the photon impact point on the entrance surface.

Discrepancy in the maximum collection efficiency between data and simulation is mainly due to the optical coupling between the CPC_{25° and the Power Meter probe, but also to the photon absorption in the B270 glass, to the intrinsic Power Meter probe efficiency and its dependence on the photon incident angle.

The same measurement has been repeated for several angles of incidence of photons.

This study shows as, to increase the detection surface of a SiPM by using parabolic concentrators, devices designed for small acceptance angles are preferred, with the better choice corresponding to 0° , but limiting in this way the field of view. In any case, the detection of radiation produced at fixed angles, as in experiments in which Cherenkov radiation has to be detected, can profit of this solution.

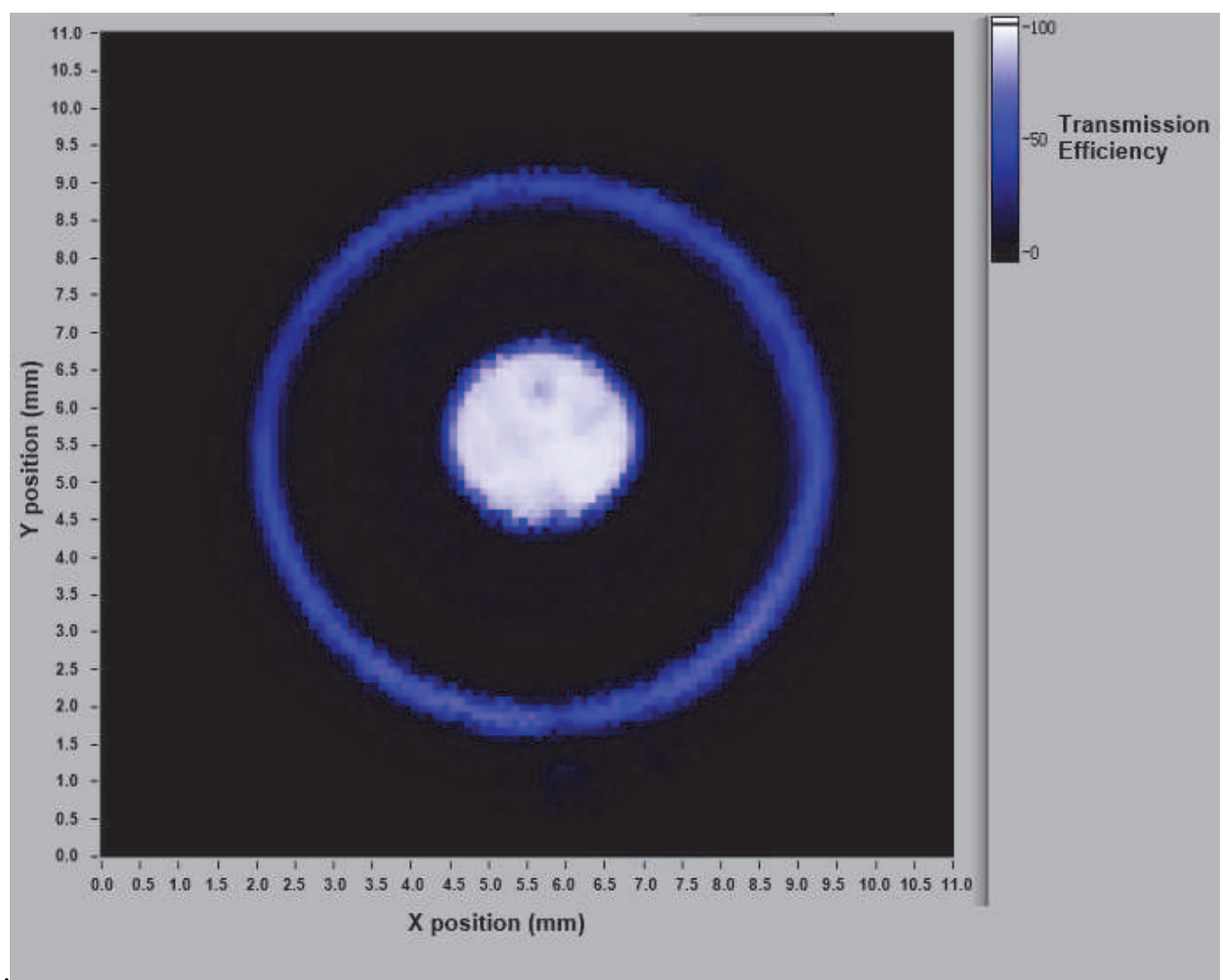


Fig. 43. Transmission efficiency on the entrance surface of the CPC_{25°}.

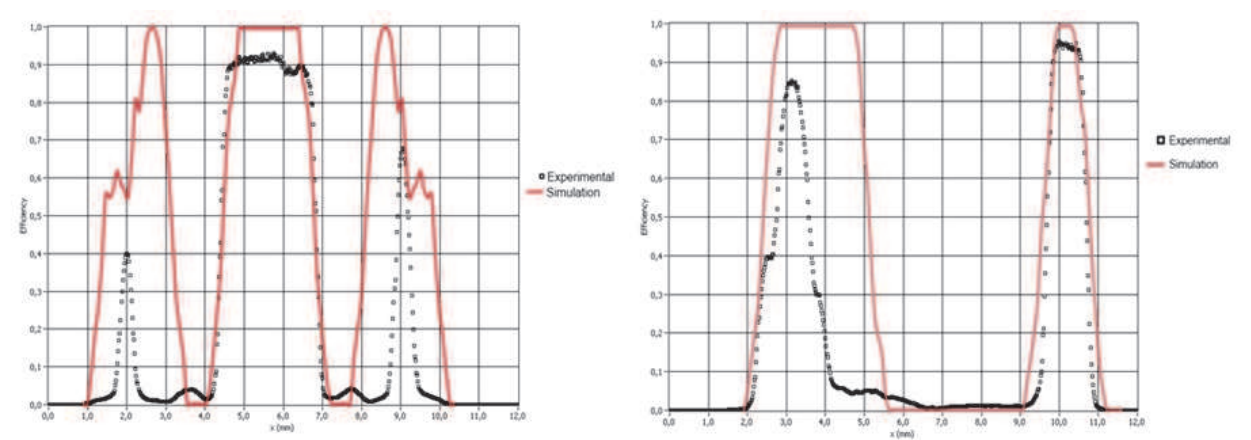


Fig. 44. Comparison between simulation and actual data on the CPC_{25°} (CPC having an acceptance angle of 25°) for impinging photons at 0° (Left) and at 20° (Right).

Differently, a pyramidal device can be considered. Simulation studies have been carried on this geometric structure (Figure 45).

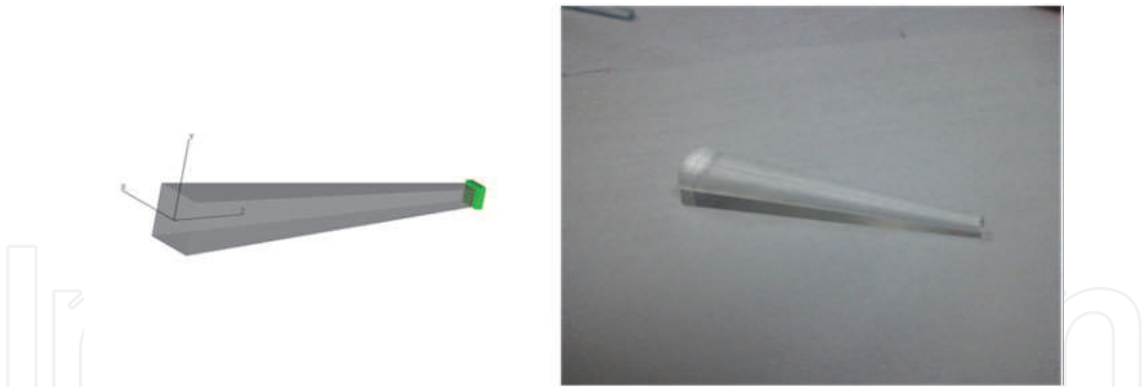


Fig. 45. 3-D model of the pyramidal concentrator used in the simulation and a photography of the pyramidal concentrator used for measurements

The pyramidal concentrator simulated in this work is an optical glass N-BK7 device, with $7.5 \times 7.5 \text{ mm}^2$ entrance surface, $2.5 \times 2.5 \text{ mm}^2$ exit surface and 50 mm long, commercially available by Edmund Optics [56]. Figure 45/right shows the pyramidal light concentrator used for the measurements.

From simulation, a good transmission efficiency, almost uniform up to 20° is obtained for this geometry, as shown in Figure 46.

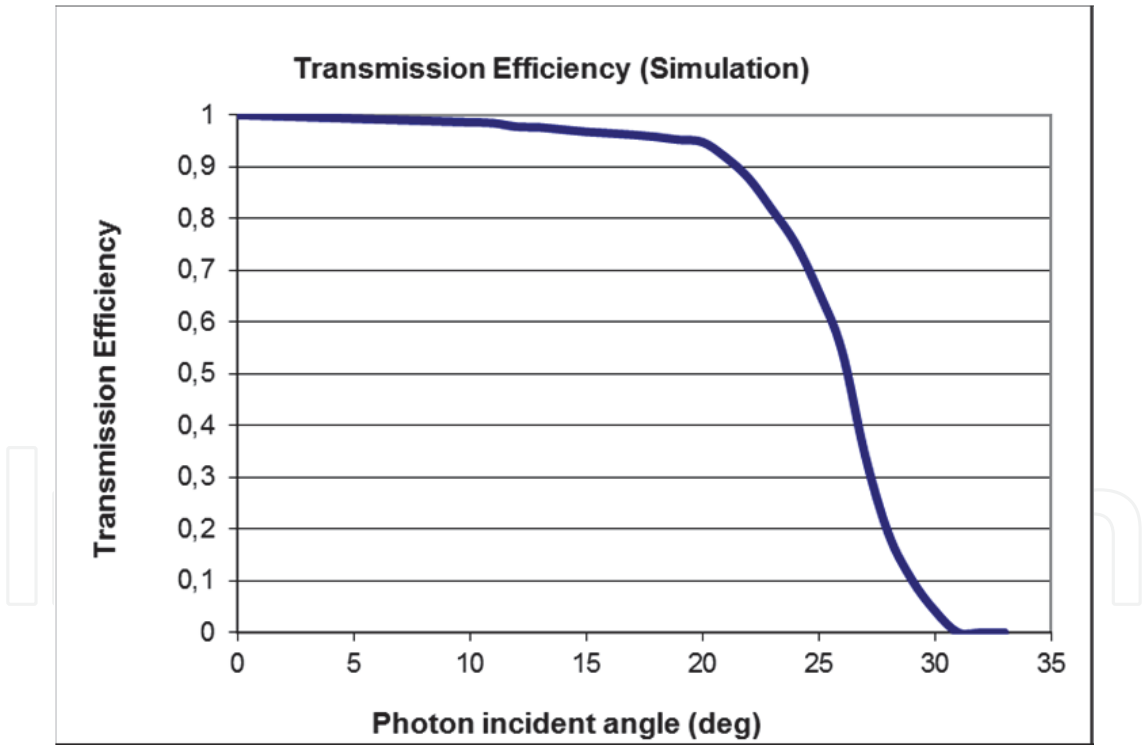


Fig. 46. Efficiency curve of the pyramidal concentrator as a function of the impinging angle of the photons.

Also for this concentrator, the efficiency has been measured as a function of the impact position on the entrance surface, by using the experimental set-up described in Figure 42. The transmission efficiency measured is shown in Figure 47, Figure 48 and Figure 49 for different incident angles.

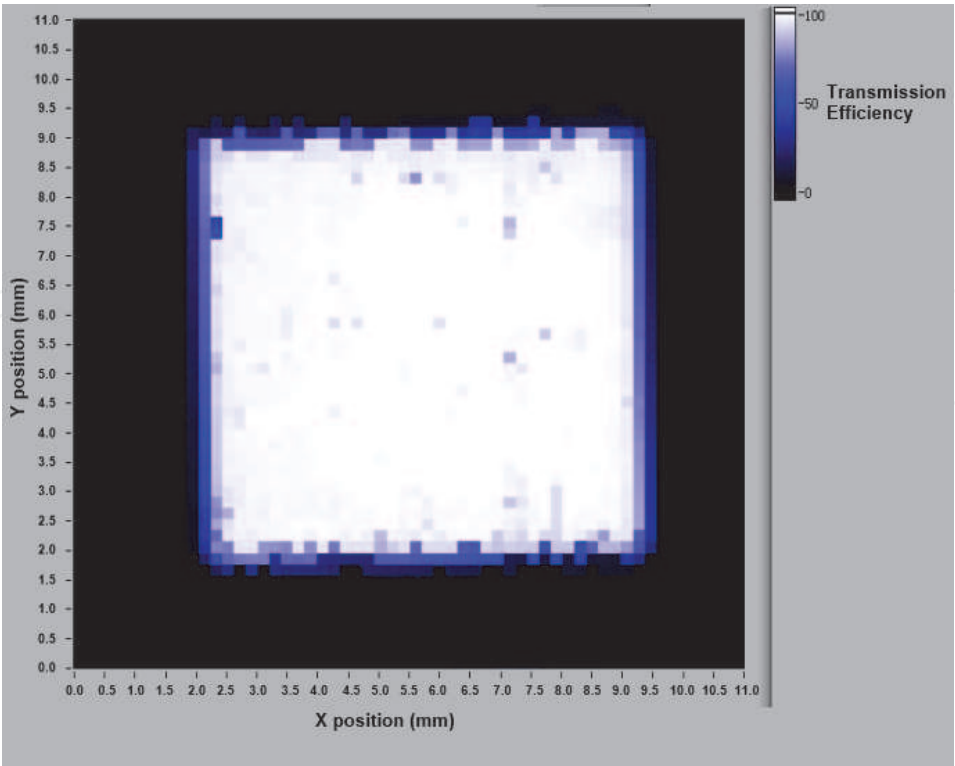


Fig. 47. Measurement of the transmission efficiency on the entrance surface of the pyramidal concentrator for 0° impinging photons.

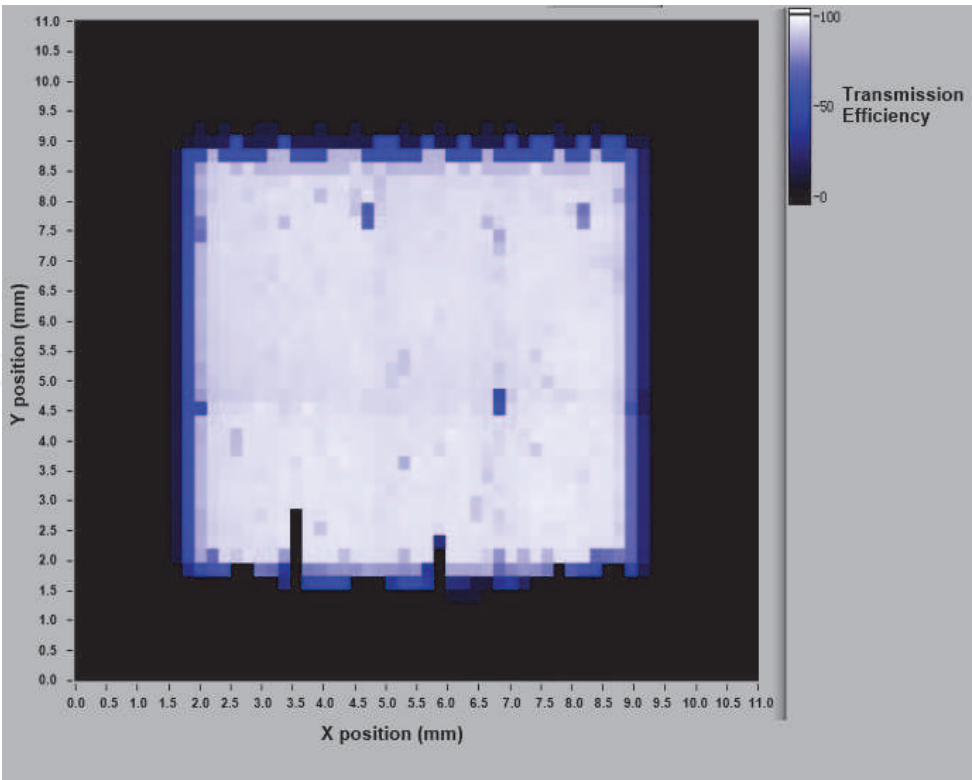


Fig. 48. Measurement of the transmission efficiency on the entrance surface of the pyramidal concentrator for 5° impinging photons.

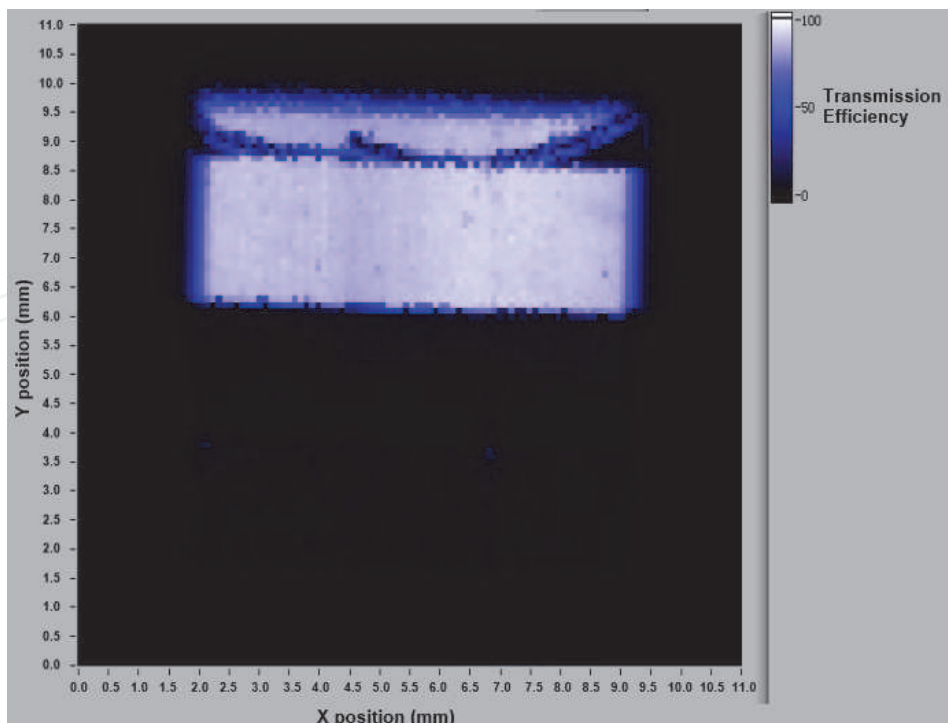


Fig. 49. Measurement of the transmission efficiency on the entrance surface of the pyramidal concentrator for 10° impinging photons.

Measurement results show that transmission efficiency of such a pyramidal light concentrator has a slight dependence on the impact point except for the case of incident angles of 10°. In fact, as shown in Figure 49, in this case large part of the entrance surface (about an half) results in a very low efficiency (about 10%). Actually, this partial inefficiency may be due to the very large angles of exiting photons (>60°), out of the angular acceptance of the Power Meter probe.

A second methods adopted to evaluate the effect of light concentrators is based on the measurement of photons detected with a 3x3 mm² MPPC S10931-025P by Hamamatsu arranged at the exit surface of the concentrator (Figure 50).

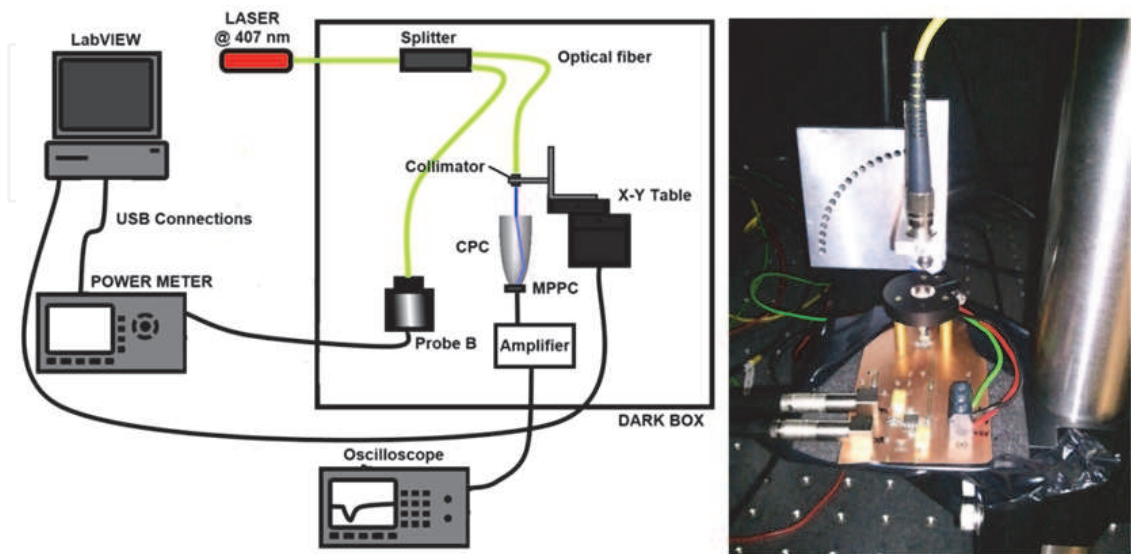


Fig. 50. The experimental set-up: light concentrator on the MPPC

The average number of incident photons on the concentrator, can be determined by measuring the laser power on one of the two outputs of the splitter. The MPPC signal, amplified by the National Semiconductor LMH6624 chip as already described, has been measured on the oscilloscope and an estimation of the overall efficiency of the system (light concentrator + MPPC) has been done by evaluating the number of photons detected by the MPPC. Laser power has been set to 40 photons per pulse on the surface of the CPC_{25°}, with an incidence angle of 0°. The maximum total efficiency for several distances of impact point from the center along one diameter (Figure 51) has been measured. Results show that a maximum obtainable efficiency is 0.1, while observing dynamic range it is possible to note that this shape of concentrator is not useful to increase the field of view of a MPPC.

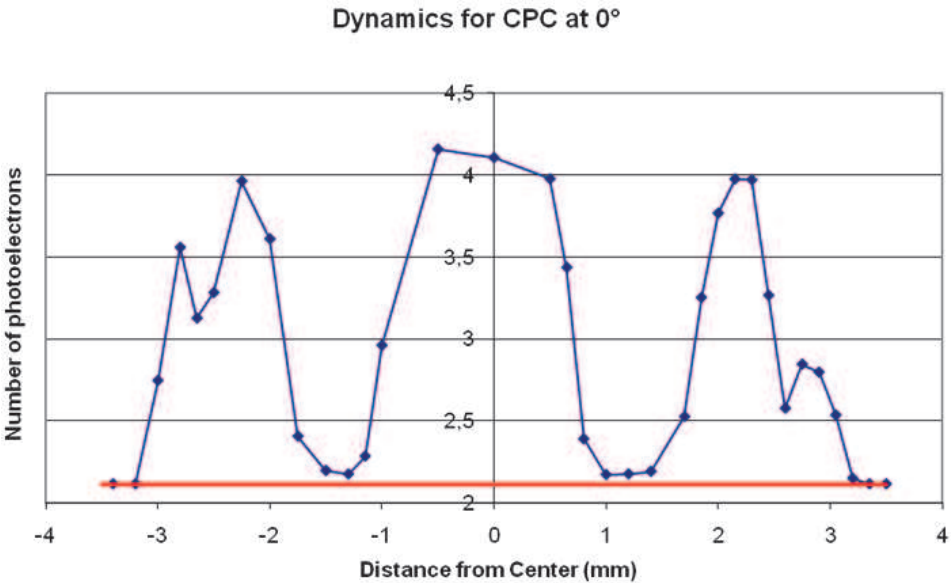


Fig. 51. Number of photoelectrons as a function of the distance of impact point from the centre
The same experimental set-up has been used to measure the efficiency of pyramidal concentrator (see Figure 52).

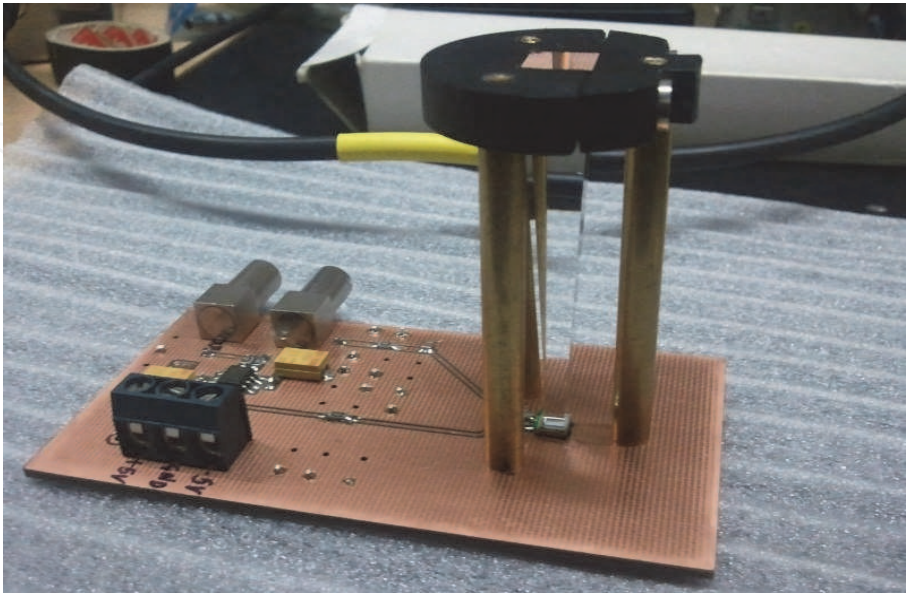


Fig. 52. Experimental set-up for pyramidal concentrator using an MPPC as a sensitive device.

Figure 53 shows the efficiency measurement for several distance of impact point from the center (along one dimension) and for several incident photon angles. Again it can be observed that the maximum total efficiency is 0.1, but in this case the total surface is enhanced. Furthermore, the efficiency results to be very uniform for incident angles in the range 0°-10°. The efficiency of the concentrator will be surely enhanced by developing SiPMs in which a front-side structure with quenching resistors is integrated into the silicon bulk. In this mode obstacles for light like metal lines or contacts, can be omitted and therefore the fill factor would only be limited by the gaps indispensable for the optical cross-talk suppression and it can reach in principle 100% [57]. Being the fill factor of present SiPM of the order of 30% (see Figure 13 and Figure 16) and taking into account it represent the main contribution to the concentrator efficiency, it will be possible to achieve very interesting overall efficiencies of the order of 35-40%. In this way, the features of a SiPM and concentrator can largely overcome the properties of the classical PMT.

8. Hybrid photo detectors

One option to further improve the angular coerture of a silicon device could be to combine it with vacuum technology. One can replace the dynodes structure of a photomultiplier with a silicon photodiode (HPD - Hybrid Photo Detector or with an avalanche photodiode (HAPD - Hybrid Avalanche Photo Detector). The detection of photon starts as in an ordinary photomultiplier at the photocathode, where a photoelectron is produced.

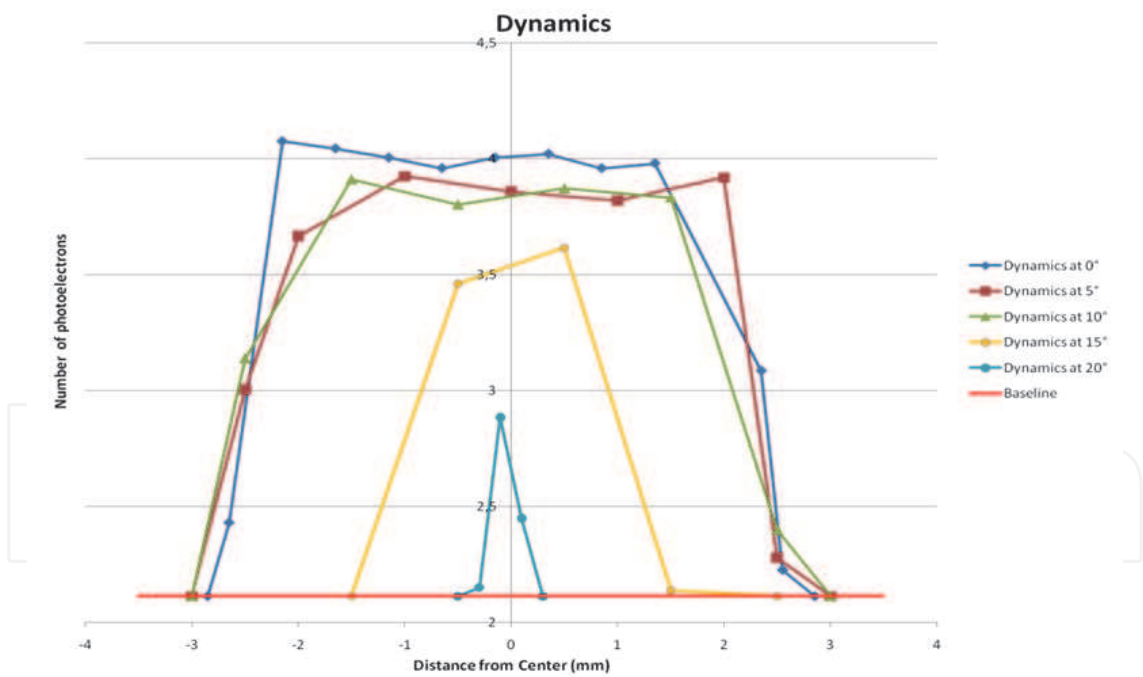


Fig. 53. Efficiency measurement for several distance of impact point from the center (along one dimension) and for several angles of the incident photon.

A pioneering configuration using a gain $G = 1$ p-i-n diode has been proposed 10 years ago by Hamamatsu and DEP. Using p-i-n diodes the signal amplification is given by the number of electron-hole pairs produced by electrons emitted from the photocathode, accelerated by a high-intensity electric field and injected into the target diode. The gain depends on the energy of incident photoelectrons: at 4 kV operational voltage, about 1100

electron-hole pairs are generated. However, in many applications where an higher sensitivity is required, such a small gain (further reduced by the photocathode QE) limits the low level light detection capability.

More recently, a gain improvement was obtained using diodes in avalanche regime (APD), with a resulting additional gain of ~ 20 – 50 . The overall photomultiplier gain increases, yet not enough for low light level detection. In addition, the fluctuations in the avalanche multiplication, limit the useful gain range.

The idea, which starts from these experience and from the consolidation of the Geiger-APDs, is to combine them into a sort of classical vacuum tube: electrons emitted by a photocathode can be collected and focused on an array of G-APDs, which acts as the amplifier. The junction works as an electron multiplier with a gain of 10^5 – 10^6 , equivalent to the dynode chain of a classical VPMT. Thus the Vacuum Silicon Photomultiplier Tube (VSiPMT) would consist of the following:

- a photocathode for photon-electron conversion,
- an electric field to accelerate and focus the photoelectrons on a small area covered by the G-APD array,

With 10 kV between photocathode and SiPM, the range of 10 keV photoelectrons impinging on the silicon is $1.5\ \mu\text{m}$ (as shown in Figure 32). In a conventional front illuminated n^+pp^+ structure, the n^+ layer has to be enough shallow ($\leq 0.5\ \mu\text{m}$) in order to have an efficient ionization in the p region. With standard equipment for detector fabrication, layers with a junction depth of 100 nm can be obtained [32]. In addition the high-field region should be as thin as possible in order to have more ionization beyond it, maximizing the electron trigger probability. Otherwise, at lower voltages, a junction structure p^+nn^+ is needed. The ionization should happen in the p^+ side allowing electrons to pass the whole high-field zone with high avalanche efficiency. In both cases photoelectrons spend most of the ionization within the p layer thickness. In contrast with the photon detection, the precise range of the photoelectrons permits the optimization of the thickness of the junction n^+pp^+ or p^+nn^+ layers, minimizing the depletion region with great advantage for lowering the dark current, increasing at same time the efficiency and the time resolution.

Recently C. Joram and al. at CERN [58] performed a very interesting study concerning the response of SiPM devices to the electrons impinging. Results they found have been so encouraging and interesting to influence also the title they give to the article: “Proof of principle of G-APD based hybrid photo detectors”. In practice they demonstrate the feasibility of such a solution, already preannounced by our group in [2]. The CERN group, thanks to their usual activities, had the possibility of making a detailed test just dedicated to this aspect. We consider their result as a precious confirmation of our previous theories concerning this arrangement.

Exploiting the full fill factor of a front illuminated SiPM described in a previous paragraph, an ultimate design for a new semiconductor hybrid photomultiplier is possible. It consists of a hemispherical vacuum tube with a deposited photocathode and a special SiPM in which quenching resistor and electric contacts are integrated in the bulk. The admittance of such a component on the sensitive surface allows the full geometrical efficiency of a SiPM used as amplifying element, making it very attractive also in this application. So in this way this hybrid PMT results equivalent to those, already existing, manufactured with APD (gain 10^2), but with a gain comparable to the standard PMT (10^6 – 10^7).

In conclusion, photoelectrons emitted by the photocathode are accelerated, focused and then amplified by Geiger junctions (Vacuum Silicon PhotoMultiplier, VSiPMT). Such an

amplifier, which would substitute the classical dynode chain, presents several attractive features such as small size, low cost, high gain, high efficiency, absence of an external voltage divider, no power consumption, weakened dependence on magnetic fields.

These developments will offer an attractive response to the necessity of increasing active surfaces with high sensitivity.

8.1 SiPM in cryogenics

As a last point we wish to underline the possible applications of SiPMs in cryogenic environments. Both SiPM matrices and VSiPMTs can be considered as a promising alternative to classical photomultipliers for VUV scintillation detection in liquid noble gas experiments requiring a high sensitivity to very low energies to detect neutralino Dark Matter signals (see for instance [59, 60]). The drop of thermal noise at low temperatures, three orders of magnitude at -95° for liquid Xenon, enhances the linearity and the single photon detection capability. The above considerations regarding the front and back illuminated SiPM induce to envisage a quantum efficiency of 25% in VUV region [61]. These figures encourage the use of these new devices in cryogenic environment [62].

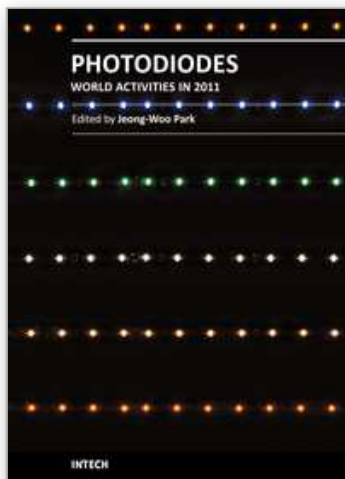
9. Conclusions

The so-called silicon photomultipliers (SiPMs, MPPCs by Hamamatsu, etc.) are already replacing photomultiplier tubes in many applications. Recently this new photon detector is operative on different R&D lines in various applications. High performances characterize such a device: reduced dimensions, high gain, low power supply, single photon sensitivity, magnetic field operation, very good time resolution, low cost. In particular low power supply and negligible power consumption together with a single photon counting, make it very interesting also in hostile environments (space, astronomy) and suitable for a wide variety of applications (including medicine and biology). The drawback of this detector are the reduced dimensions limited by the dark count and silicon cost. To collect photons both from great surfaces or/and volumes and to increase the field of view of such a photo detector, three solutions have been presented in this paper. Apart the classical and proven technique of detecting scintillation light from large volume using WLS fibers, which diameter dimensions are compatible with the active part of the present commercial SiPM, two innovative solutions are presented to improve the field of view and/or focus the light: cones and pyramidal light concentrators assembled in single SiPM or organized in a matrix shape. Such a device are applied both to read Cherenkov detector on beam experiments (RICH) and astronomical telescopes. A second solution simplifies and improves the classical PMT performances by replacing the dynode amplification chain with a SiPM in a Hybrid configuration. A similar photo detector using a lower APD gain has been implemented and it is already operative. There is space to implement both solutions. To do this at the best, advanced SiPM have to be realized. Two are the critical features that have to be solved in the next years: the dark noise reduction and the elimination of the dead region around the microcell (fill factor) where the quenching resistor is positioned. Already today it has been proposed a front-side illuminated detector structure with quenching resistors integrated into the silicon bulk. In this concept, the fill factor is only limited by the gaps necessary for optical cross-talk suppression. Compared to existing devices the proposed detector has the potential of a very high photon detection efficiency.

10. References

- [1] J. Ninkovic, Nucl. Instr. and Meth. A 580 (2007) 1020.
- [2] G. Barbarino et al., A new high-gain vacuum photomultiplier based upon the amplification of a Geiger-mode p-n junction., Nucl.Instrum.Meth.A594:326-331,2008.
- [3] Pamela: A payload for Antimatter Matter Exploration and Light-nuclei Astrophysics. P. Picozza et al. Published in Astropart.Phys.27:296-315,2007.
- [4] An anomalous positron abundance in cosmic rays with energies 1.5-100 GeV., O. Adriani et al., Nature 458:607-609,2009.
- [5] Moon and sun shadowing effect in the MACRO detector. MACRO Collaboration (M. Ambrosio et al.) Astropart.Phys.20:145-156,2003.
- [6] Final results of magnetic monopole searches with the MACRO experiment. MACRO Collaboration (M. Ambrosio et al.), Eur.Phys.J.C25:511-522,2002.
- [7] Limits on dark matter WIMPS using upward going muons in the MACRO detector. MACRO Collaboration (M. Ambrosio et al.). Phys.Rev.D60:082002,1999.
- [8] NEMO Collaboration, Sensitivity of an underwater Cerenkov km**3 telescope to TeV neutrinos from Galactic Microquasar., Astropart.Phys.28:1-9,2007.
- [9] First results from a Dark Matter search with liquid Argon at 87 K in the Gran Sasso Underground Laboratory, P. Benetti et al., Astropart.Phys.28:495-507,2008, e-Print: astro-ph/0701286
- [10] WARP liquid argon detector for dark matter survey, Presented by C. Rubbia at the 6th UCLA Symposium on Sources and Detection of Dark Matter and Dark Energy in the Universe. Published in New Astronomy Reviews Volume 49, Issues 2-6, May 2005, Pages 265-269
- [11] The MAGIC Telescope and the observation of gamma ray bursts, MAGIC Coll. (Denis Bastieri et al.), Nuovo Cim.28C:711-714,2005, e-Print: astro-ph/0504310
- [12] Very high energy photons from distant extragalactic sources observed by MAGIC: AGNs and GRBs., MAGIC Coll. AIP Conf.Proc.1018:157-166,2008.
- [13] Warp liquid argon detector for dark matter survey, WARP Coll. New Astron.Rev.49:265-269,2005.
- [14] Characterization of ETL 9357FLA photomultiplier tubes for cryogenic temperature applications., A. Ankowski et al., Nucl.Instrum.Meth.A556:146-157,2006.
- [15] Performance and behavior of photomultiplier tubes at cryogenic temperature, M. Prata et al., NIMA567(2006) 222.
- [16] Detection of VUV light at high quantum efficiency with large area avalanche photodiodes (LAAPDs) R. Chandrasekharan et al., Nucl.Instrum.Meth.A567:45-47,2006.
- [17] Detection of the VUV liquid argon scintillation light by means of glass-window photomultiplier tubes, P. Benetti, et al., Nucl.Instrum.Meth.A505:89-92,2003.
- [18] The recent development and study of silicon photomultiplier, V. Savelev, Nucl.Instrum.Meth.A535:528-532,2004.
- [19] Development of the First Prototypes of a Silicon PhotoMultiplier (SiPM) at ITC-irst., N. Dinu et al., Nucl.Instrum.Meth.A572:422-426,2007
- [20] Photon counting techniques with silicon avalanche photodiodes -Appl. Opt., H.Dautet et al., 32 (1993) 3894-3900.
- [21] D.Renker Nuclear Instruments and Methods in Physics Research A 567 (2006) 48-56.
- [22] Limited Geiger-mode microcell silicon photodiode: New results, G. Bondarenko et al. Nucl.Instrum.Meth.A442:187-192,2000.
- [23] Silicon photomultiplier and its possible applications, P. Buzhan et al., Nucl.Instrum.Meth.A504:48-52,2003.

- [24] Novel type of avalanche photodetector with Geiger mode operation, V. Golovin et al., Nucl.Instrum.Meth.A518:560-564, 2004.
- [25] A.N. Otte et al., Nucl.Instrum.Meth.A567:360-363, 2006.
- [26] Glenn F. Knoll: Radiation Detection and Measurement John Wiley & Sons, Inc.
- [27] S.O.Kasap, Optoelectronics and Photonics, Principles and Practices, Prentice-Hall International (2001)
- [28] <http://www.pveducation.org/pvcdrom>
- [29] M.A.Greenand, M.J.Keevers, Progress in Photovoltaics: Research and Applications, Vol. 3, Issue3 313 (1995) 189.
- [30] D.Renker,Nucl.Instrum.Meth.A468 (2002) 164.
- [31] William J. Price, Nuclear Radiation Detection McGraw-Hill Book Company.
- [32] C. Piemonte, Nucl. Instr. and Meth. A 568 (2006) 224.
- [33] P. Buzhan, B. Dolgoshein, et al., An advanced study of silicon photomultiplier, ICFA Instrumentation Bulletin, 2001.
- [34] MPPC Data Sheet, Hamamatsu Photonics K. K., <http://www.hamamatsu.com>.
- [35] R.J. McIntyre, J. Appl. Phys. 32 (6) (1961) 983.
- [36] R.H. Haitz, J. Appl. Phys. 35 (5) (1964) 1370.
- [37] M. Yokoyama et al., Development of Multi-Pixel Photon Counters, SNIC Symposium, Stanford, California, April 2006.
- [38] S. Gomi et al., 2006 IEEE Nuclear Science Symposium Conference Record
- [39] J. Haba, Status and Perspectives of Pixelated Photon Detector (PPD), Nucl. Instrum. Meth. Phys. Res A, 595, 154-160 (2008).
- [40] W.G.Oldham IEEE Transactions On Electron Devices, Vol. Ed-19, No. 9, September 1972.
- [41] S. Adachi, Phys. Rev. B 38 (1988) 12966.
- [42] J. Humlíček, et al., J. Appl. Phys. 65 (7) (1989) 2827.
- [43] H.R. Philipp, E.A. Taft, Phys. Rev. 120 (1960) 37.
- [44] R. Hartmann, et al., Nucl. Instr. and Meth. A 387 (1997) 250.
- [45] G. Collazuol, et al., Nucl. Instr. and Meth. A 581 (2007) 461.
- [46] K. Amako, et al., KEK-PREPRINT-2005-28, May 2005, 8pp. (published in IEEE Trans. Nucl. Sci. NS-52 (2005) 910.).
- [47] [/www.cern.ch/geant4](http://www.cern.ch/geant4)
- [48] D. Ferenc et al., Nucl. Instr. and Meth. A 567 (2006) 166.
- [49] A. Lacaita et al., Photon-assisted avalanche spreading in reach-through photodiodes, Appl. Phys.Lett. 62 (1993) 606.
- [50] A. Vacheret et al, arXiv1101.1996
- [51] M. Yokoyama et al., Nucl. Instr. and Meth. A 610 (2009) 128
- [52] A.A. Radu et al., Nuclear Instruments and Methods in Physics Research A 446 (2000) 497-505
- [53] F. Lucarelli et al., Nuclear Instruments and Methods in Physics Research A 589 (2008) 415-424
- [54] K. Bernlöhr et al., Astroparticle Physics 20 (2003) 111-128
- [55] R. Winston, W.T. Welford, High Collection Nonimaging Optics, Academic Press, New York, 1989.
- [56] www.edmundoptics.com
- [57] J.Ninkovic et al., Nuclear Instruments and Methods in Physics Research A 617 (2010) 407-410.
- [58]: C. Joram, A.Rudge, J. Séguinot: Nucl. Instr. and Meth. A 621 (2010) 171-176.
- [59] WARP Collaboration, Astropart. Phys. 28 (2008) 495.
- [60] XENON Collaboration, Phys. Rev. Lett. 100 (2008) 021303.
- [61] J. Ninkovic, et al., Nucl. Instr. and Meth. A 580 (2007) 1013.
- [62] E. Aprile, Nucl. Instr. and Meth. A 556 (2006) 215.



Photodiodes - World Activities in 2011

Edited by Prof. Jeong Woo Park

ISBN 978-953-307-530-3

Hard cover, 400 pages

Publisher InTech

Published online 29, July, 2011

Published in print edition July, 2011

Photodiodes or photodetectors are in one boat with our human race. Efforts of people in related fields are contained in this book. This book would be valuable to those who want to obtain knowledge and inspiration in the related area.

How to reference

In order to correctly reference this scholarly work, feel free to copy and paste the following:

Giancarlo Barbarino, Riccardo de Asmundis, Gianfranca De Rosa, Carlos Maximiliano Mollo, Stefano Russo and Daniele Vivolo (2011). Silicon Photo Multipliers Detectors Operating in Geiger Regime: an Unlimited Device for Future Applications, Photodiodes - World Activities in 2011, Prof. Jeong Woo Park (Ed.), ISBN: 978-953-307-530-3, InTech, Available from: <http://www.intechopen.com/books/photodiodes-world-activities-in-2011/silicon-photo-multipliers-detectors-operating-in-geiger-regime-an-unlimited-device-for-future-applic>

INTECH
open science | open minds

InTech Europe

University Campus STeP Ri
Slavka Krautzeka 83/A
51000 Rijeka, Croatia
Phone: +385 (51) 770 447
Fax: +385 (51) 686 166
www.intechopen.com

InTech China

Unit 405, Office Block, Hotel Equatorial Shanghai
No.65, Yan An Road (West), Shanghai, 200040, China
中国上海市延安西路65号上海国际贵都大饭店办公楼405单元
Phone: +86-21-62489820
Fax: +86-21-62489821

© 2011 The Author(s). Licensee IntechOpen. This chapter is distributed under the terms of the [Creative Commons Attribution-NonCommercial-ShareAlike-3.0 License](https://creativecommons.org/licenses/by-nc-sa/3.0/), which permits use, distribution and reproduction for non-commercial purposes, provided the original is properly cited and derivative works building on this content are distributed under the same license.

IntechOpen

IntechOpen